High-Temperature Oxidation Behavior of TaTiCr, Ta_4Ti_3Cr, Ta_2TiCr, and Ta_4TiCr_3 Concentrated Refractory Alloys

Noah J. Welch[a,b,c*], Maria J. Quintana[a,b,c], Todd M. Butler[d], Peter C. Collins[a,b,c]

[a.] *Department of Materials Science and Engineering, Iowa State University, Ames, IA 50011, USA*

[b.] *Center for Advanced Non-Ferrous Structural Alloys (CANFSA), USA*

[c.] *Ames Laboratory, Iowa State University, Ames, IA, 50011, USA*

[d.] *Air Force Research Laboratory, Materials and Manufacturing Directorate, Wright-Patterson Air Force Base, OH 45433, USA*

**corresponding author: njwelch@iastate.edu*

Abstract

This study reports the unique microstructures and high-temperature oxidation behavior of TaTiCr, Ta_4Ti_3Cr, Ta_2TiCr, and Ta_4TiCr_3 concentrated refractory alloys and elucidates the effect of moderate composition changes on oxidation performance. All alloys investigated in this study formed *bcc* solid solution matrices with second phase Laves precipitates (except for Ta_4Ti_3Cr, being single-phase *bcc).*The alloys were tested for 24 hours at 1200°C, of which: TaTiCr exhibited superior oxidation performance for the duration of the test; Ta_4TiCr_3 showed moderate oxidation resistance, with both parabolic and linear kinetic regimes; and Ta_4Ti_3Cr and Ta_2TiCr both exhibited poor oxidation performance, with Ta_2TiCr being completely oxidized after testing. All alloys formed complex oxides; however, the excellent performance of the TaTiCr alloy can be attributed to the compact, continuous nature of the oxide scale, the combination of complex oxides and protective Cr_2O_3 formation, and the complex internal nitride morphology, slowing oxygen ingress and reducing the depth of internal oxidation.

Keywords: high-temperature, oxidation, refractory, TaTiCr, complex oxide

1. Introduction

Research of refractory alloys started in the 1950s with the aim to develop structural alloys that could maintain their mechanical properties at high temperatures. Much of the focus centered around processability. In the last decade, another wave of research has taken place with the objective to identify potential refractory metallic materials that exceed the operational temperature limits of Ni-base superalloys (>1100°C) [1]. This is partially due to the major difference in alloy melting temperatures when comparing state-of-the-art Ni-base superalloys (~1400°C) with refractory alloys (~1800°C) [1–3] However, a major challenge with refractory alloys is their high susceptibility to oxidation, which makes them primarily reliant on protective coatings and/or limits their use to environments where oxygen is minimized [4,5]. Outside of coatings, one promising alternative is to improve the native oxidation resistance of refractory alloys through concentrated alloying additions. These alloys are known as refractory high-entropy alloys (RHEAs) and refractory complex concentrated alloys (RCCAs) [2,6,7]. The compositional complexity of these alloys facilitates the formation of complex oxides due to the reaction between simple native oxides. These oxides serve to suppress the non-protective effects of deleterious simple oxides (e.g. Ta_2O_5) by preferentially forming more complex species (e.g. $CrTaO_4$) and ultimately

promote sluggish oxidation kinetics [2,8]. RCCAs are of primary interest due to their unique combinations of properties. The compositional complexity has shown to give rise to unique properties. Some RCCAs have been reported to maintain their high strength at high temperatures [9] as well as exhibit improved oxidation resistance. Despite their promise, the low room-temperature ductility and high density still remain a challenge in some systems.

As reported elsewhere in the literature [2,3,10], alloys based upon Ta, Ti, and Cr are attractive candidates for structural applications at high temperatures. However, the majority of published research has focused only on binary systems, such as CrNb or CrTa [11–20], or simple alloys with small additions of Si, Ni, Co, Fe, Al and Re [11,15,16]. Although Ta has a rather high density (16.65 g/cm^3), the TaTiCr system was chosen for this work because Cr and Ti have been shown to form moderately protective complex oxides when present with Ta [2] and their lower elemental densities (7.19 g/cm^3 and 4.51 g/cm^3, respectively) will positively impact the specific properties. There exists a relatively substantial body of research into the high-temperature oxidation performance of Cr(X)+Cr_2X alloys (X is Nb or Ta) [11–14] which show that such alloys form microstructures where the continuous matrix phase is a Laves phase with solid solution particles dispersed throughout. Given that the target service temperature for these alloys is at least 1100 °C (to exceed the temperature window of Ni-based superalloys), Butler et al. [3,10] have reported oxidation and mechanical behavior in the ternary and quaternary space, investigating CrNb, CrNbTi and CrNbTaTi RCCAs at 1200°C. They have shown that the addition of Ti to the binary CrNb alloy changes the microstructural evolution, effectively "inverting" the microstructure from one with a Laves matrix to one with a *bcc* matrix with dispersed Laves particles, improving the ductility substantially. The complex oxide $CrTaO_4$ was reported in the Cr-Ta system by Brady, et al. [14] as well as the TaMoCrTiAl system by Gorr and Schellert, et al. [21,22] and the MoTaTiCr system by Li, et al. [23] and has been attributed to providing a large degree of protection if the scale is continuous, compact, and adherent. Although complex oxides such as $CrTaO_4$ can be very protective, there have not been any strong links established between microstructure and oxidation performance and, further the compositional influence on microstructure morphology in concentrated refractory alloys. Ta-rich binary compositions in combination with high concentrations of Ti have been investigated only regarding microstructural characterization and mechanical properties [24].

This work explores the role of Ta, Ti, and Cr alloying additions to the resulting microstructures and oxidation behavior of a series of novel Ta-Ti-Cr alloys (TaTiCr, Ta_4Ti_3Cr, Ta_2TiCr, and Ta_4TiCr_3). The equiatomic alloy (TaTiCr) is considered to be a true RCCA, the other three concentrated alloys were chosen with 50 at% Ta and varying ratios of Ti and Cr. These four compositions were strategically chosen to systematically compare the relative ratios of alloying additions on Laves phase fraction and matrix composition. CALPHAD predictions showed that increasing the Cr:(Ta+Ti) ratio directly increased the relative Laves fraction, and vice versa. The predictions also show a strong dependence on matrix composition with the relative Ta:Ti ratio in the alloys. The microstructures are explored, both experimentally and through CALPHAD based models, to provide insight into the validity of commercial, refractory alloy databases. The 1200°C oxidation kinetics of each alloy are quantified and linked to microstructural changes in the alloy and resulting oxide scales, providing useful insights on the active oxidation mechanisms for each alloy and identifying promising candidates for further exploration.

2. Methods

Ingots of TaTiCr, Ta_4Ti_3Cr, Ta_2TiCr, and Ta_4TiCr_3 (Fig. 1 and Table 1) were vacuum-arc melted from high purity powders (99.995%) at the Ames Laboratory Metals Preparation Center facilities. Each ingot was prepared on a water-cooled copper hearth and flipped several times to promote homogeneity. After casting, and to ensure chemical uniformity in the specimens, ingots were wrapped in Ta foil and homogenized by Hot Isostatic Pressing (HIP) for 3 hours at 1400°C and 207MPa under a high-purity Ar atmosphere. Heating/cooling rates were ~15°C/min. HIPing was performed by the Materials and Manufacturing Directorate, Air Force Research Laboratory, at Wright-Patterson Air Force Base.

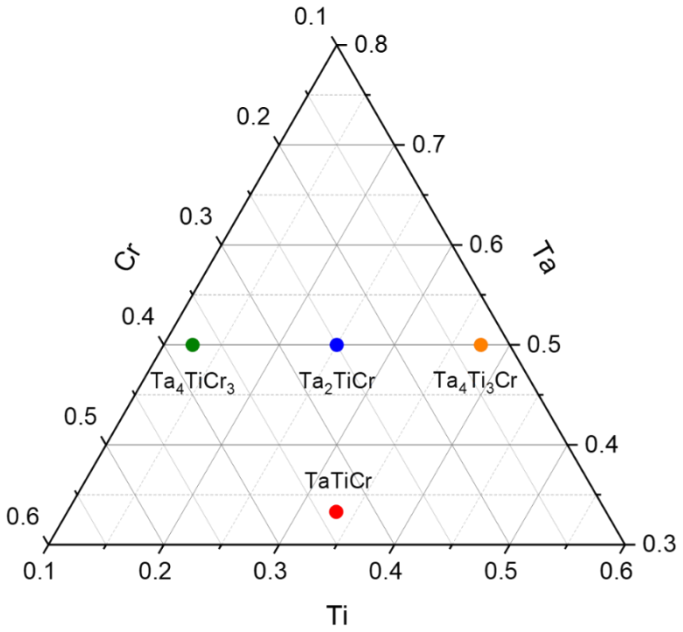

Figure 1: Ternary phase diagram in at% of the Ta-Ti-Cr system with the four selected alloys plotted.

Table 1: Nominal (i.e., target) and experimentally achieved compositions of the selected alloys at%.

Alloy		**Ta**	**Ti**	**Cr**
TaTiCr	nominal	33.3	33.3	33.3
	experimental	30.6	36.8	32.6
Ta_4Ti_3Cr	nominal	50.0	37.5	12.5
	experimental	50.9	37.2	11.9
Ta_2TiCr	nominal	50.0	25.0	25.0
	experimental	46.5	22.5	31.0
Ta_4TiCr_3	nominal	50.0	12.5	37.5
	experimental	49.9	12.2	37.9

Densities of the four alloys were determined using the Archimedes method to a high degree of accuracy [25]. An Ohaus Adventurer Analytical balance (10^{-5} g) was used to measure the mass of the HIP ingots once in air (m_{air}) and again while submerged in deionized water (m_{water}). The densities were then calculated using Eq. (1), where the effect of air buoyancy is corrected for by including the air density at room temperature (ρ_{air} = 1.19 g/cm^3):

$$\rho = (\rho_{water} - \rho_{air}) \frac{m_{air}}{m_{air} - m_{water}} + \rho_{air}$$

(1)

Oxidation tests were conducted using a Netzch Jupiter 449 F3 simultaneous thermal analysis (STA) thermal analyzer. Due to constraints associated with the size of the crucible, 3mm x 3mm cylindrical specimens were excised from the HIP ingots using Electrical Discharge Machining (EDM). To remove the EDM re-cast layers, all specimens were pickled for 600 seconds using a solution consisting of 20 ml HF, 80 ml HSO_3, 20 ml HNO_3, and 40 ml H_2O [26]. In preparation for oxidation testing, the pickled specimens were placed in alumina crucibles on top of a layer of calcined alumina powder to avoid reaction with the crucible for the duration of the tests. All oxidation tests were performed at 1200°C for 24 h, with a heating rate of 30°C/min. An additional 13-hour test was performed for the Ta_2TiCr alloy since it had completely oxidized after the original 24-hour test. Specimens were subjected to a continuous flow of bottled air atmosphere at 80 ml/min with a 10 ml/min N_2 balance[1]. Specimen mass was continuously recorded during oxidation tests to report specific mass change with respect to initial surface area (mg/cm^2). To further investigate the nature of the oxide structures in the earliest stages of oxide formation, as well as to verify the complete oxidation tests performed in the thermal analyzer, 1- and 24-hour box furnace tests were performed on HIP specimens placed in alumina crucibles.

Subsequently, the as-cast, HIP, and oxidized specimens were hot mounted in a conductive phenolic resin, ground and polished using conventional metallographic techniques. To ensure that the polished surfaces of the specimens were deformation-free, the metallographically-prepared specimens were polished through a 0.04 µm colloidal silica finish, then etched with a solution of 20 ml HF, 20 ml HNO_3, and 60 ml H_2O to selectively etch/reveal any residual deformation associated with prior scratches, and subsequently polished (vibratory polisher) with 0.04 µm colloidal silica solution for 18 hours.

Microstructural analysis of the as-cast, HIP, and oxidized specimens were conducted using a combination of scanning electron microscopy (SEM) and energy dispersive X-ray spectroscopy (EDS). Samples were imaged using both an FEI Teneo LoVac SEM and an FEI Inspect F50 SEM equipped with both conventional secondary and backscattered electron detectors, as well as with an Oxford X-max EDS detector. EDS was conducted on both the oxide free surface, as well as cross-sections through the oxides to better interpret external and internal oxidation thicknesses, species, and locations. Throughout this paper, all compositions are given in at%. Statistical analysis of the microstructures was performed using MIPAR image analysis software, and compared to phase fractions obtained from simulations using Pandat software (with the PanNb2018 database).

X-ray diffraction (XRD) spectra were collected from the HIP specimens, as well as from oxidized samples. Oxide scales were extracted and ground to powder. XRD scans were conducted using a Rigaku SmartLab diffractometer with Cu-Kα1 radiation (λ = 1.5406 Å) and a 2θ range of 20-80°. Post-processing of XRD data, including the calculation of the lattice parameters of the various phases, was conducted using Rigaku PDXL2 software.

[1] The 80 ml/min flow in the STA was determined by measuring specific mass change from static air box furnace tests and adjusting flow as necessary to match the static air results.

3. Results

3.1 As-cast and HIP microstructure

Backscattered electron (BSE) micrographs of the four alloys in the as-cast condition are shown in Fig. 2. The microstructure of the TaTiCr alloy (Figs. 2(a) and 2(b)) is heavily cored and consists of Ta,Ti-rich body-centered cubic (*bcc*) dendrites with fine (Ta,Ti)Cr_2 Laves precipitates in the interdendritic regions and along grain boundaries. The microstructure of the Ta_4Ti_3Cr alloy (Figs. 2(c) and 2(d)) has a *bcc* dendritic structure with no observable Laves precipitates. Similar to TaTiCr, the microstructure of the Ta_2TiCr alloy (Figs. 2(e) and 2(f)) also shows a dendritic structure with small Laves precipitates. Finally, the micrographs of the Ta_4TiCr_3 alloy (Figs. 2(g) and 2(h)) show coarse, continuous interdendritic Laves between primary *bcc* dendrites. Contrast differences in the microstructure between the dendritic and interdendritic regions (Figs. 2(a)-2(f)) are likely caused by coring, an artifact of constituent segregation during solidification. Composition differences in the dendrites were confirmed by EDS on the Ta_4Ti_3Cr alloy, where the center of the dendrite is Ta-rich (58% Ta-33% Ti-9% Cr (at%)), while the outer edge of the dendrites has a composition leaner in Ta, but richer in Ti (36% Ta-49% Ti-15% Cr (at%)). BCC dendrites and fine Laves precipitates suggests a hypoeutectic composition, with solidification starting with BCC precipitation and growth, followed by Laves nucleation. Ta_4TiCr_3 is likely closer to the eutectic composition since the Laves is the continuous phase and of similar morphology to the BCC dendrites.

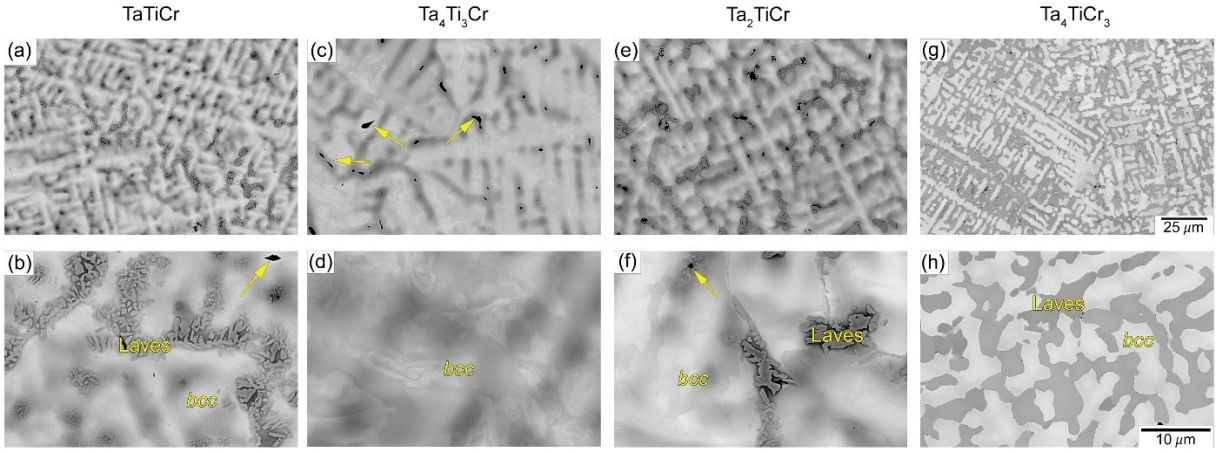

Figure 2. Backscatter SEM micrographs of the as-cast microstructure of the four alloys: (a,b) TaTiCr, (c,d) Ta_4Ti_3Cr, (e,f) Ta_2TiCr, (g,h) Ta_4TiCr_3. Arrows indicate porosity. Scale bars are the same for all figures within each horizontal row.

Following the HIP cycle (3 hours at 1400 °C and 207 MPa), the microstructure of the TaTiCr alloy (Figs. 3(a) and 3(b)) was found to exhibit a Ti-rich *bcc* matrix with coarsened C15 Laves particles dispersed throughout the microstructure. The XRD data supports this assessment (Fig. 4), as it exhibits prominent peaks associated with a disordered *bcc* (A2) and cubic C15 Laves. The lattice parameters of the *bcc* phase and Laves phase in the TaTiCr alloy are 325.7 pm and 702.4 pm, respectively. The similarity in contrast between the *bcc* and Laves in this alloy is due to the high Ti content in the *bcc* phase. Since Ti and Cr have similar Z-values (atomic numbers 22 and 24, respectively), when imaged using

backscattered electrons, the two phases have less contrast than the other alloys which have more high-Z Ta (atomic number 73) content in the matrix, resulting in high contrast between the two phases in backscattered electron micrographs. In addition, features that are consistent with twin boundaries (or other disruptions in stacking) can be seen in the Laves particles (Fig. 3b) and are likely explained by high-temperature hexagonal C14 Laves transforming into C15 upon cooling [27,28]. Although the TaTiCr alloy is not predicted to form C14 from CALPHAD, the Ta-Cr and Ti-Cr system both form C14 independently, so the compositional gradients present in the as-cast state suggest that C14 may be stabilizing after arc-melting and subsequently transforming into C15 during the HIP process. The measured phase fractions from the TaTiCr alloy coincide with those obtained from the calculated phase diagram (Fig. 5(a), Table 2) at a temperature of ~600 °C, suggesting that further transformation is kinetically restricted during the slow cooling from the HIP temperature (1400 °C) to room temperature. When comparing experimental and simulated phase compositions, the experimental compositions of the *bcc* phase is notably Cr-rich and the Laves phase is Cr-lean and Ti-rich. The deviation from the predicted phase compositions may be caused by Ti substitution on the Cr sublattice in the C15 Laves cell, since Cr and Ti have similar atomic radii (176 and 166 pm, respectively). The phase diagrams (Fig. 5) also predict a eutectoid hexagonal close packed (*hcp*) phase transformation below 600 °C, which is not seen in either micrographs or XRD data, further suggesting sluggish transformation kinetics at lower temperatures. Similar results were reported by Butler et al. [9] for the NbCrTi and NbCrTaTi systems, where the predicted *hcp* phase was not observed after HIP.

The microstructure of the Ta_4Ti_3Cr alloy (Figs. 3(c) and 3(d)) evolved into a uniform, single-phase Ta-rich *bcc* structure after HIP, with a composition near the nominal alloy chemistry (Table 2). The XRD data supports the interpretation of single-phase microstructure (Fig. 4), containing peaks only associated with *bcc*. The lattice parameter of the *bcc* phase in the Ta_4Ti_3Cr alloy was determined to be 324.6 pm. As seen in the calculated phase diagram for this alloy (Fig. 5(b)) the lower Cr content results in a higher *bcc* phase fraction and, consequently, a lower Laves phase fraction. Contrary to the phase diagrams, the Ta_4Ti_3Cr alloy did not contain any Laves or *hcp* –predicted to form at 1277°C and 575°C, respectively– suggesting that the diffusion-controlled Laves and *hcp* phase transformations are restricted during the slow cooling from the HIP temperature (1400°C) to room temperature. The density of the Ta_4Ti_3Cr alloy was determined to be 11.79 g/cm^3.

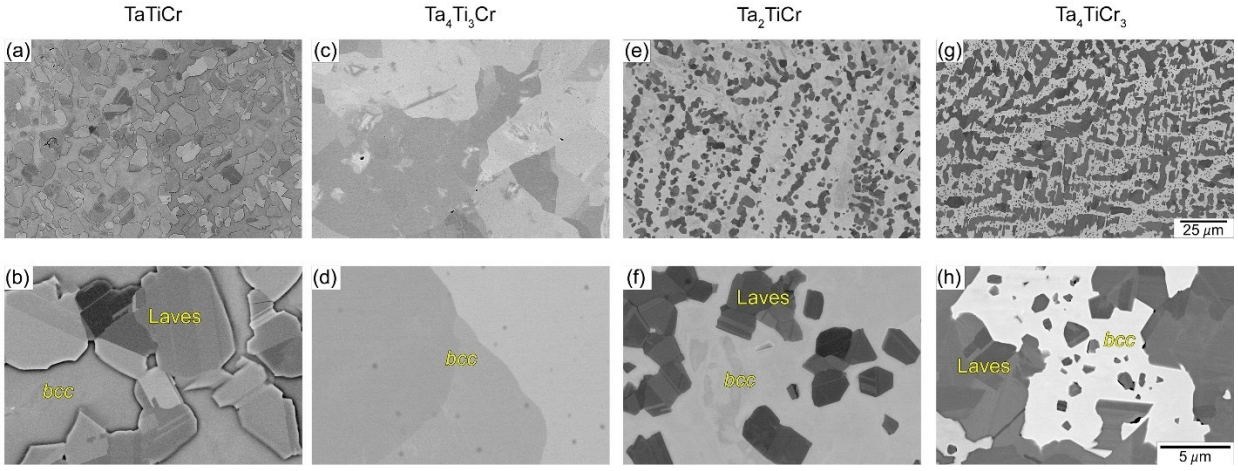

Figure 3. Backscatter SEM micrographs of the microstructure of the four alloys after HIP for 3 hours at 1400°C and 207MPa: (a,b) TaTiCr, (c,d) Ta_4Ti_3Cr, (e,f) Ta_2TiCr, and (g,h) Ta_4TiCr_3. Scale bars are the same for all figures within each horizontal row.

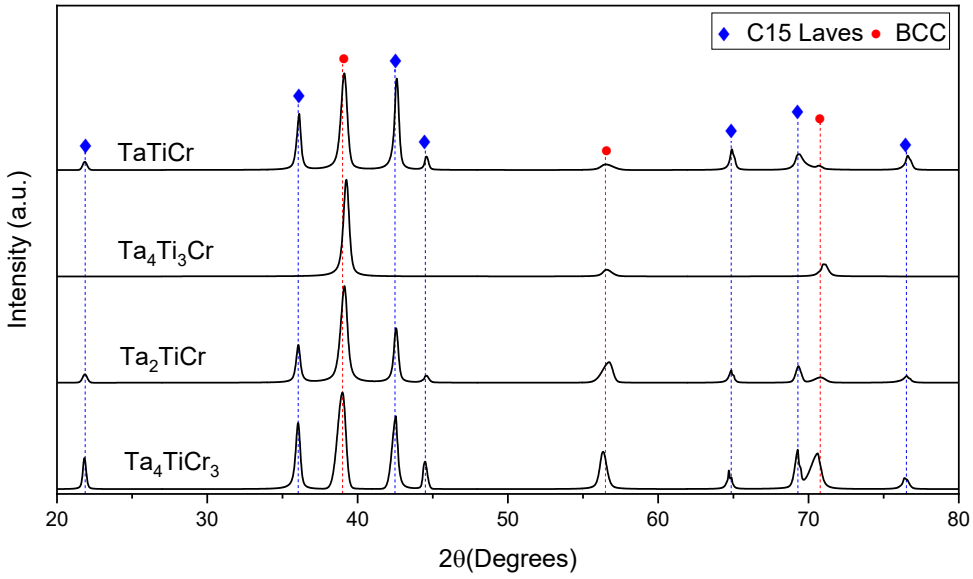

Figure 4. XRD spectra collected from the TaTiCr, Ta_4Ti_3Cr, Ta_2TiCr, Ta_4TiCr_3 alloys after HIP.

Similar to the microstructure observed for the Ta_4Ti_3Cr alloy, the dendritic structures in the matrix of the Ta_2TiCr alloy homogenized into a uniform, Ta-rich *bcc* structure after HIP (Figs. 2(e) and 2(f)). The fine Laves precipitates present after casting coarsened into blocky, polygonal particles present both along grain boundaries and within the grains. XRD data (Fig. 4) for this alloy shows sharp peaks associated with these two phases. The lattice parameters of the *bcc* phase and Laves phase in the Ta_2TiCr alloy were determined to be 325.1 pm and 703.6 pm, respectively. The calculated phase diagram for the Ta_2TiCr alloy (Fig. 5(c), Table 2) suggests a higher equilibrium phase fraction of the Laves phase than present in the Ta_4Ti_3Cr alloy due to higher Cr content, which is supported by the stereologically measured Laves phase fraction of 0.34. The equilibrium phase fractions and compositions near 1000°C correspond to the measured data, suggesting that further transformation was suppressed below that temperature. As with the other alloys, the *hcp* phase is expected to form at lower temperatures (555°C) and was not experimentally observed. The density of the Ta_2TiCr alloy was determined to be 11.95 g/cm^3.

The morphology of the continuous Laves structure of the Ta_4TiCr_3 alloy coarsened and became more faceted after HIP (Figs. 3(g) and 3(h)), likely due to the C14→C15 Laves transformation mentioned previously. Additionally, secondary Laves particles nucleated in the Ta-rich *bcc* regions between the Laves dendrites, likely due to the decrease in Cr solubility in the matrix during cooling from 1400°C (Table 2). XRD data (Fig. 4) for the Ta_4TiCr_3 alloy shows defined Laves and *bcc* peaks. The Cr content in each alloy and the Laves peak intensities generally correlate to the Laves fraction present (Table 2), e.g., the Ta_2TiCr alloy has a weaker Laves signature compared to the Ta_4TiCr_3 alloy. The lattice parameters of the *bcc* phase and Laves phase for the Ta_4TiCr_3 alloy are 326.4 pm and 704.7 pm, respectively. Much like the Ta_2TiCr alloy, the experimental phase fraction and composition data from the calculated phase diagram (Fig. 5(d), Table 2) match with the equilibrium phase fractions and compositions at 1000°C. Again, the *hcp* phase, expected to form at 480°C, was not experimentally observed. The density of the Ta_4TiCr_3 alloy is the highest of the four, and was determined to be 12.69g/cm^3. Notably, the densities of

the Ta-rich alloys (Ta_4Ti_3Cr, Ta_2TiCr, and Ta_4TiCr_3) are quite high, potentially limiting their practical use in aerospace applications; however, these high-density compositions are integral to understanding the behavior of the Ta-Ti-Cr system in its entirety.

Table 2. EDS and simulated phase fraction and composition for the TaTiCr, Ta_4Ti_3Cr, Ta_2TiCr, and Ta_4TiCr_3 alloys (at.%)

Alloy	Density (g/cm^3)	Method*	Phase	Fraction	Composition		
					Cr	Ta	Ti
TaTiCr	8.40	Experimental	*bcc*	0.51	12.1	28.1	59.8
			Laves	0.49	58.8	27.3	13.9
		Simulated (600°C)	*bcc*	0.51	1.6	36.0	62.4
			Laves	0.49	66.6	30.5	2.9
Ta_4Ti_3Cr	11.79	Experimental	*bcc*	1.0	11.9	50.9	37.2
			Laves	0.0	-	-	-
		Simulated (1400°C)	*bcc*	1.0	12.5	50	37.5
			Laves	0.0	-	-	-
Ta_2TiCr	11.95	Experimental	*bcc*	0.66	12.3	45.1	42.6
			Laves	0.34	57.4	31.6	11
		Simulated (1000°C)	*bcc*	0.68	5.5	59.9	34.6
			Laves	0.32	66.4	28.9	4.7
Ta_4TiCr_3	12.69	Experimental	*bcc*	0.48	11.9	67.2	20.9
			Laves	0.52	57.9	34.8	7.3
		Simulated (1000°C)	*bcc*	0.47	4.6	72.4	23.0
			Laves	0.53	66.3	30.4	3.3

*Experimental phase fraction was measured after HIP.
Simulated phase fractions were obtained from data from Pandat PanNb2018.

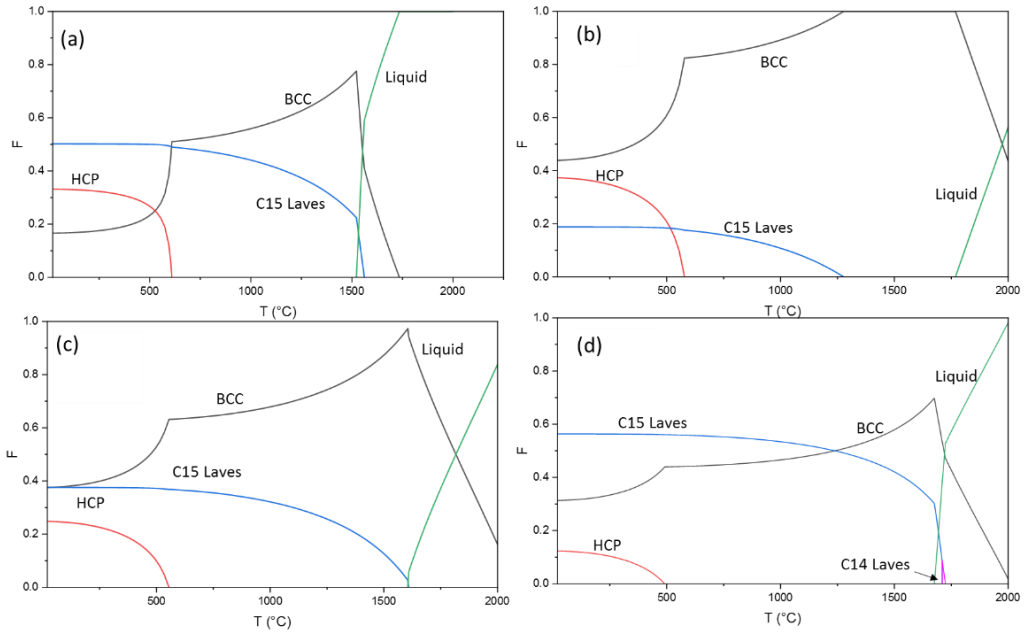

Figure 5. Calculated phase fraction versus temperature diagrams for the (a) TaTiCr, (b) Ta_4Ti_3Cr, (c) Ta_2TiCr, and (d) Ta_4TiCr_3 alloys, using Pandat and PanNb2018 database.

3.2 Oxidation Behavior

A plot of the oxidation kinetics and pre- and post-oxidation photographs of the samples for each alloy is shown in Fig. 6. The alloy with the slowest oxidation kinetics was TaTiCr, with a specific mass change of 7.2 mg/cm^2 after 24 hours at 1200°C. The TaTiCr alloy was qualitatively observed to have a relatively thin oxide scale that was dark grey, with brown regions along the edges of the cylinder. The other alloys (Ta_4TiCr_3, Ta_4Ti_3Cr, and Ta_2TiCr) had specific mass changes of 71.5, 124.1, and 160.9 mg/cm^2, respectively. The Ta_4TiCr_3 specimen had a dark green, rumpled scale that bulged slightly in the middle of the cylinder. The Ta_4Ti_3Cr specimen showed a thick, cracked orange scale that contained longitudinal splits along the length of the specimen. The Ta_2TiCr specimen was completely oxidized after 24 hours and had a thick brown scale that left no remaining metal after testing. The total mass gain is representative of the net behavior of oxidation, nitridation, and volatilization [29]. The kinetic data of the four alloys was analyzed using a variation of the general growth rate law:

$$\Delta m = k\, t^n \qquad (2)$$

where Δm is the specific mass change normalized to initial surface area (mg/cm^2), k is the rate constant, t is the oxidation time and n is the time exponent. Oxidation kinetics with $n = 1$ are considered to be linear and primarily rate-limited by metal-oxide interface reactions. When $n = 0.5$, the material is considered to have parabolic kinetics, where the rate is diffusion-controlled either by the outward diffusion of cations, the inward diffusion of anions, or a combination of the two types. Intermediate exponents between 1 and 0.5 are indicative of mixed mode behavior, involving both diffusion- and

interface-controlled mechanisms. Sub-parabolic kinetics below n = 0.5 are indicative of diffusion-controlled reactions in tandem with volatilization effects, e.g. cubic kinetics where n = 0.3 [28].

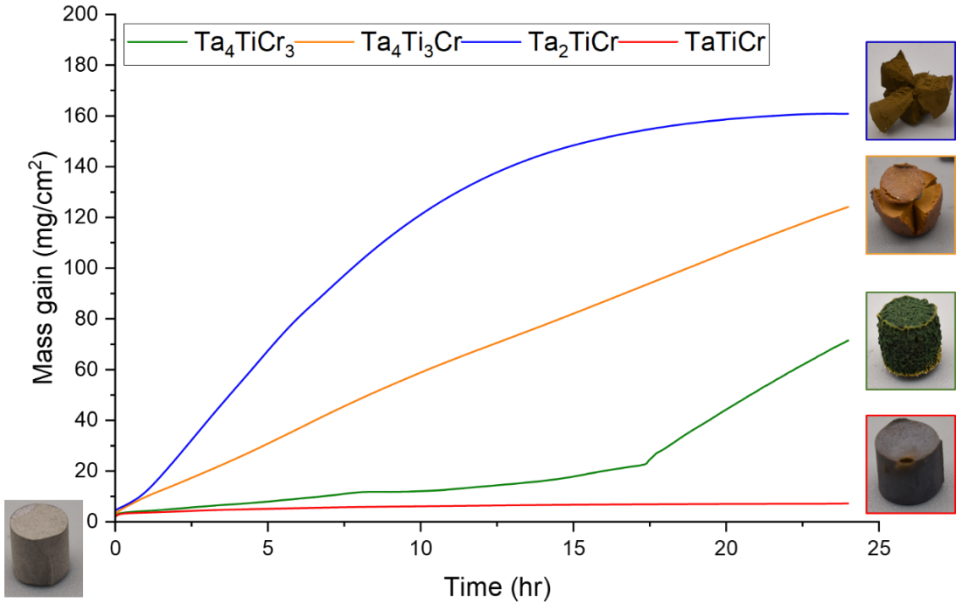

Figure 6. Specific mass change during the 1200 °C STA oxidation tests of TaTiCr, Ta_4Ti_3Cr, Ta_2TiCr, Ta_4TiCr_3. Specimen images were taken after 24 hours.

The TaTiCr alloy showed one distinct near-cubic regime of kinetics for the duration of the test with n = 0.23 and k = 3.58 mg/cm^2-h$^{-0.23}$. Both Ta_4Ti_3Cr and Ta_2TiCr alloys primarily display singular near-linear regimes of oxidation (n = 0.85, k = 7.88 mg/cm^2-h$^{-0.85}$, and n = 1.03, k = 12.06 mg/cm^2-h$^{-1.03}$, respectively); however, the kinetics of the Ta_2TiCr alloy deviate from linearity and become slower as the specimen approaches complete oxidation (after ~12 hours). The Ta_4TiCr_3 alloy exhibits a markedly different behavior compared to all other alloys, starting with a parabolic regime up to 9 hours (n = 0.51, k = 3.55 mg/cm^2-h$^{-0.51}$), followed by a near-linear regime from 9-16 hours (n = 1.17, k = 0.84 mg/cm^2-h$^{-1.17}$), and a final linear regime (n = 3.19, k = 0.01 mg/cm^2-h$^{-3.19}$) until the end of the test (24 hours). The multi-regime kinetic behavior seen in the Ta_4TiCr_3 alloy indicates a shift in the oxidation mechanism and is characteristic of breakaway oxidation, highly influenced by the initial volatility of oxide species [30], which will be discussed in detail in Section 3.3.4.

3.3 Post-Oxidation Microstructures

X-ray diffraction spectra captured from the oxide scale powder of the four alloys after 24 hours are shown in Fig. 7. Several mixed "rutile" (P42/mnm, space group (SG) 136) complex oxide structures were observed in all alloys, including: $(Cr,Ta,Ti)_2O_4$ which was observed in all four alloys (Fig. 7(a)-7(d)); $TaTiO_4$ which was seen in the TaTiCr, Ta_4Ti_3Cr, and Ta_2TiCr alloys(Fig. 7(a)-7(c)); TiO_2 which was seen in the TaTiCr and Ta_4Ti_3Cr alloys (Fig. 7(a)-7(b)); $CrTaO_4$ which was seen in the Ta_2TiCr and Ta_4TiCr_3 alloys (Fig. 7(c)-7(d)); and $CrTiO_4$ which was only seen in the TaTiCr alloy (Fig. 7(a)). Previously, similar mixed structures have been observed in the CrNbTi and CrNbTaTi system by Butler, et al. [3] and were reported to be caused by competitive oxide formation driven from the high concentration of alloying additions, ultimately leading to shared occupancy within the rutile cation sublattice. Additionally, peaks associated with Cr_2O_3 (R-3c, SG 167) were seen in the TaTiCr and Ta_4TiCr_3 alloys (Fig. 7(a), 7(d)). The Ta_2O_5 (I/4mmm, SG 139) oxide was observed in all but the TaTiCr alloy (Fig. 7(b)-7(d)). The Ta_4Ti_3Cr alloy showed peaks coinciding with Ta_2TiO_7 (I 12/m 1, SG 12). Oxide products will be discussed in detail with their corresponding alloys in the following sections. These observations are presented in Table 3.

*Table 3: Alloys and oxide products identified using XRD. *Rutile structured oxide (P42/mnm, SG 136).*

Alloy	Oxide Product							
	Cr_2O_3	$(Cr,Ta,Ti)_2O_4$*	$CrTaO_4$*	$CrTiO_4$*	Ta_2O_5	$TaTiO_4$*	Ta_2TiO_7	TiO_2*
TaTiCr	x	x		x		x		x
Ta_4Ti_3Cr		x			x	x	x	x
Ta_2TiCr		x	x		x	x		
Ta_4TiCr_3	x	x	x		x			

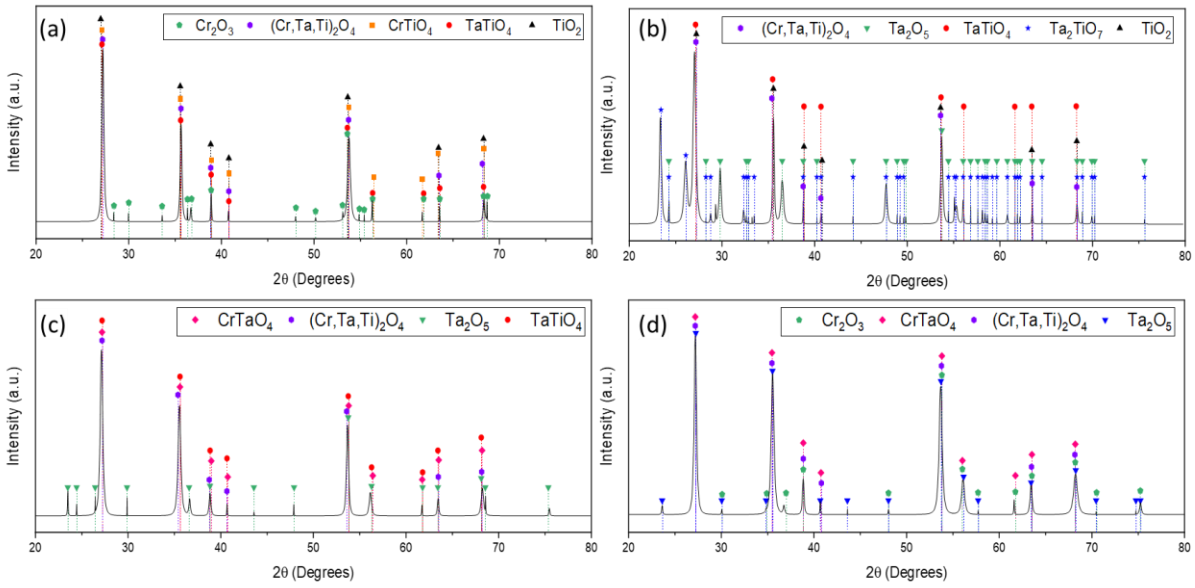

Figure 7: XRD spectra captured from the (a) TaTiCr, (b) Ta4Ti3Cr, (c) Ta2TiCr, and (d) Ta4TiCr3 alloys after oxidation at 1200 °C for 24 hrs.

3.3.1 TaTiCr Post-Oxidation

The free surface of the TaTiCr oxide scale (Fig. 8(a)) consisted of a primary TiO_2 structure (Fig. 8(a), location 1), with sporadically dispersed Cr_2O_3 clusters (Fig. 8(a), location 2). As shown by the cross-sectional view in Fig. 8(b), the TaTiCr alloy formed a multi-layered, outer oxide scale that was adherent and showed no visible spallation after 24 hours of oxidation. The outer scale thickness was 30μm. Below this outer layer, a pronounced internal reacted zone (IRZ) was observed (Fig. 8(b)). The IRZ was approximately 170μm thick and visually resembled the starting microstructure (Fig. 3(a)), with the addition of a dark, lenticular phase that formed between the Laves and *bcc* phases. The Laves particles near the metal-oxide interface (Fig. 8(c)) contained dark, titanium-rich acicular precipitates (40-60nm thick). The center (Fig. 8(d)) of the specimen remained *bcc* + Laves, with no evidence of oxide formation or any secondary effects of oxygen ingress; however, the Laves particles in the alloy core became more globular after the high temperature exposure.

The external oxide scale of the TaTiCr alloy (Figs. 8 and 9(a)) consisted of an outer titanium-rich layer (Fig. 9(a), location 1), an intermediate chromium-rich layer (Fig. 9(a), location 2), and an inner layer consisting primarily of tantalum (Fig. 9(b)) and titanium (Fig. 9(c)) with a chromium composition gradient initiating from the intermediate layer (Fig. 9(d)). Locations 1 and 2 exhibited chemistries consistent with TiO_2 and Cr_2O_3, respectively (Table 4). The innermost oxide layer exhibited multiple chemistries cascading from the Cr_2O_3 layer: $CrTiO_4$ (Fig. 9(a), location 3, Table 4), $(Cr,Ta,Ti)_2O_4$ (Fig. 9(a), location 4), and $TaTiO_4$ (Fig. 9(a), location 5; and Table 5). At the metal-oxide interface, tantalum-rich particles with chemistry similar to Ta_2O_5 (Fig. 9(a), location 6, Table 4) can be found which appear to be prior-Laves particles that have reacted after rejecting all chromium and titanium to the oxide scale. In the IRZ, the lenticular phase is titanium- and nitrogen-rich with a chemistry similar to TiN (Fig. 9(a), location 7, Table 4). The chromium-rich particles are unreacted Laves (Fig.9(a), location 8), while the *bcc* matrix (Fig. 9(a), location 9, Table 4) was tantalum -rich due to rejection of titanium from the matrix to form TiN. A Ti-rich phase with chemistry consistent with the *hcp* (α) phase is present near the internal oxidation front of the IRZ. These precipitates are likely stabilized by oxygen and nitrogen, which are two well-known α stabilizers in commercial titanium alloys [31]. Both oxygen-induced α-stabilization and a decrease in titanium solubility in the Laves phase during cooling from 1200°C are likely responsible for the acicular precipitates seen in the Laves particles near the metal-oxide interface (Fig. 8(c)), similar to other oxygen-induced changes to phase stability and solute solubility[32]. The majority of oxygen-enrichment remained in the oxide scale, with some oxygen-enrichment seen in the IRZ (Fig 9(e)), most notably segregated to Laves particles. Nitrogen-enrichment was exclusively seen in the titanium-rich regions in the IRZ (Fig. 9(f)).

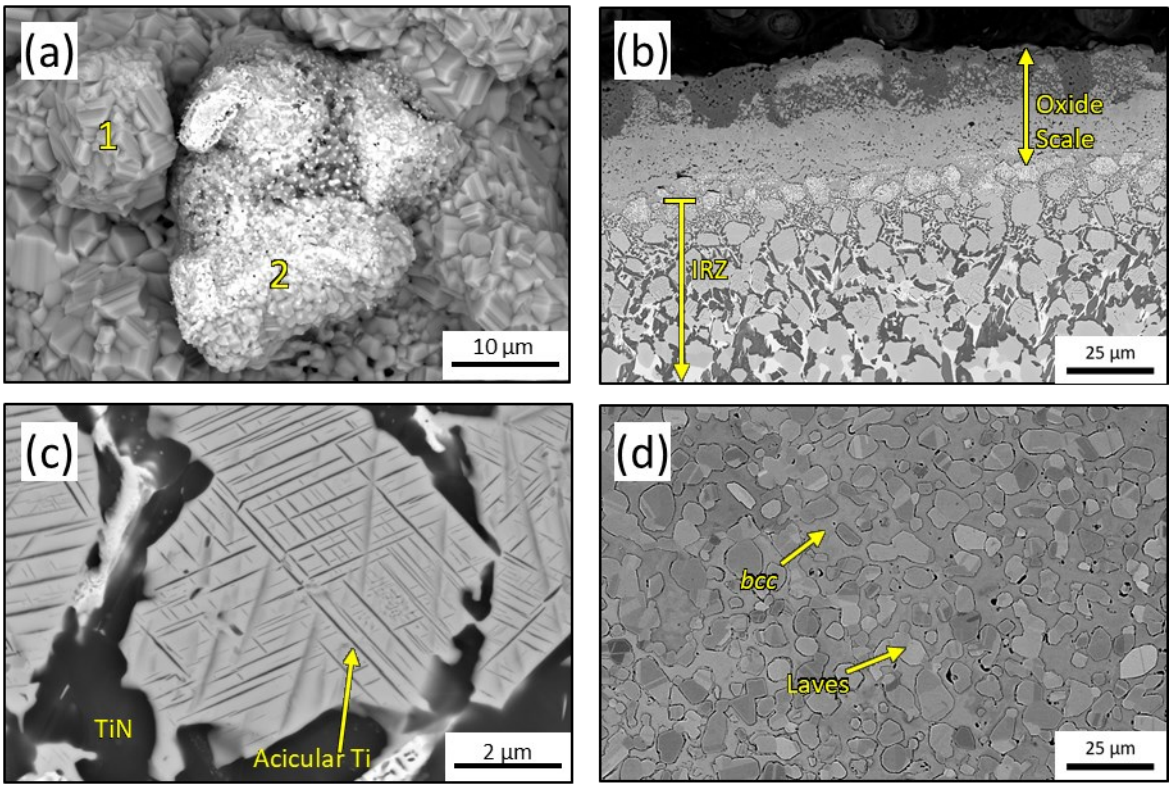

Figure 8. Backscatter SEM micrographs of the TaTiCr sample after the oxidation test (24 hours at 1200°C in air). (a) Free surface of oxide scale showing (1) TiO_2 and (2) Cr_2O_3 clusters, (b) cross-section showing IRZ and oxide scale, (c) acicular Ti nucleation in Laves particle, and (d) unreacted center of the sample.

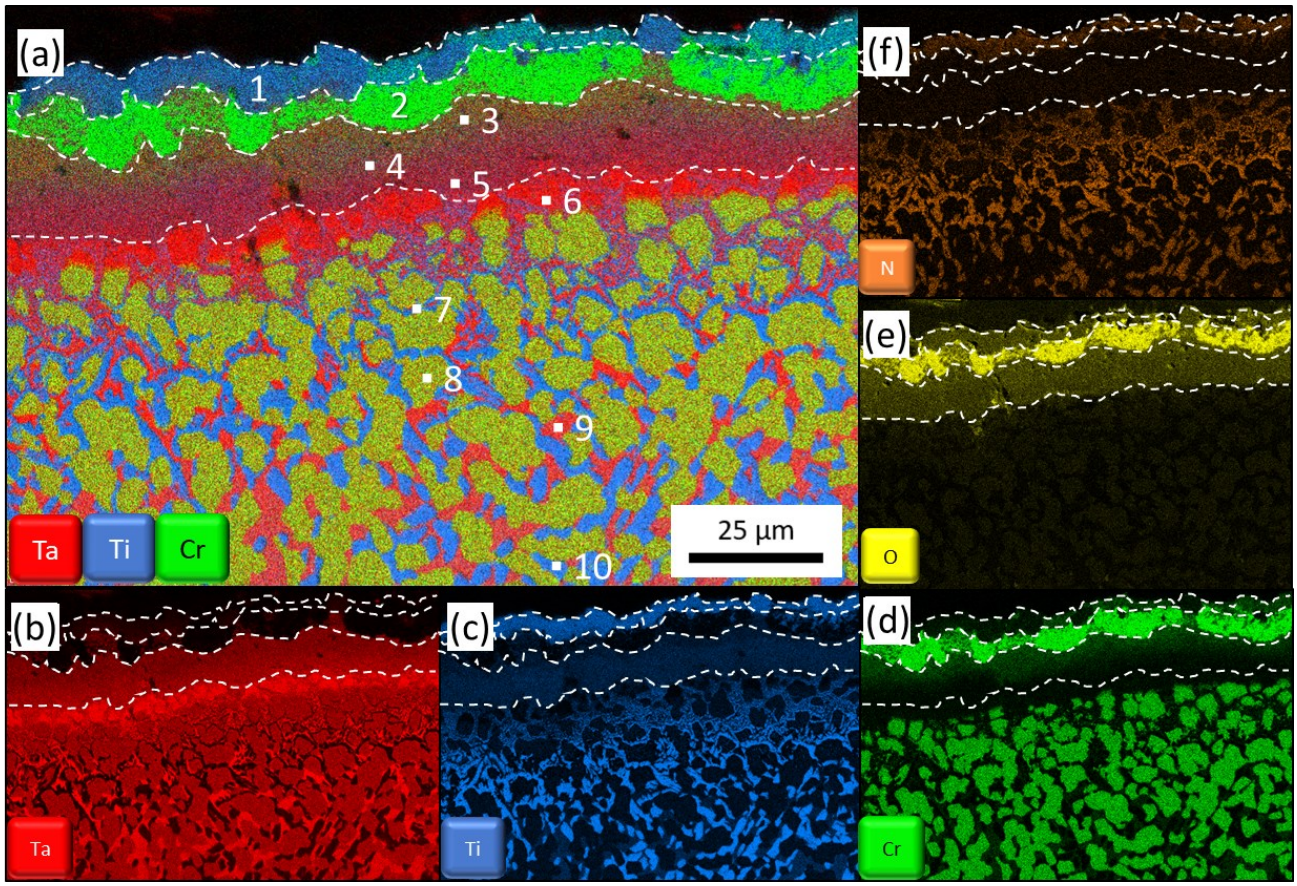

Figure 9. EDS maps of the TaTiCr alloy after 24 hrs of oxidation at 1200°C, showing (a) composite map of the alloying elements, (b) tantalum, (c) titanium, (d) chromium, (e) oxygen, (f) nitrogen content in the alloy.

Table 4. EDS measurements for the observed phases in the TaTiCr alloy after oxidation at 1200°C for 24 hrs.

Region	Fig., location	Phase	Cr	Ta	Ti	O	N
Free Surface	**8(a), 1**	TiO_2	9.2	0	26.6	64.2	-
	8(a), 2	Cr_2O_3	39.1	0.4	0.5	60.0	-
External Oxides	**9,1**	TiO_2	3.0	2.4	28.0	66.6	-
	9,2	Cr_2O_3	36.5	0.4	2.4	60.7	-
	9,3	$CrTiO_4$	7.4	0.1	27.1	65.4	
	9,4	$(Cr,Ta,Ti)_2O_4$	13.3	10.2	10.4	66.1	-
	9,5	$TaTiO_4$	-	16.2	15.4	68.4	-
IRZ	**9,6**	Ta_2O_5	0.4	24.7	4.2	70.7	-
	9,7	Laves	67.0	27.4	5.6	-	-
	9,8	*bcc*	8.4	65.8	25.9	-	-
	9,9	TiN	2.5	3.5	41.4	-	52.6
	9,10	*hcp*	0.5	5.8	79.7	6.3	7.7

3.3.2 Ta_4Ti_3Cr Post-Oxidation

As noted previously, the XRD data of the Ta_4Ti_3Cr scale powder indicated the presence of Ta_2O_5 and Ta_2TiO_7. Both of these oxides are known to be non-protective oxides in other refractory alloys [33]. The free surface of the oxide scale (Fig. 10(a)) was uniform and consisted primarily of rutile TiO_2. The Ta_4Ti_3Cr alloy cross section (Fig. 10(b)) shows the formation a thick porous oxide scale, measuring 1.29mm. Near the internal oxide-metal interface (Fig. 10(b)), dark, needle-like precipitates grew during the oxidation tests with a very fine morphology within the grains (Fig 10(c)). Coarser precipitates were observed along grain boundaries (Fig 10(c)), continuing towards the center of the specimen (Fig. 10(d)) and suggesting the entire internal area had reacted to some extent. Further, fine Laves precipitates (Fig 10(c)) were seen along the coarse grain boundary precipitates near the metal-oxide interface.

The outer oxide scale of the Ta_4Ti_3Cr alloy (Fig. 11(a)) consisted of a seemingly repeating structure whose morphology transitions to resemble that of the post-oxidation microstructure near the metal-oxide interface (Fig. 11(b)). The bulk of the oxide consists of three distinct oxide structures. Within this figure, location 1 in the scale was measured to have a chemistry consistent with Ta_2TiO_7 (Fig. 11(a), Table 5); the Ta-rich "pockets" in location 2 were measured to be Ta_2O_5 (Fig. 11(a), Table 5), while the repeating structure in location 3 was measured to be $(Cr,Ta,Ti)_2O_4$ (Fig. 11(a), Table 5). The repeating morphology is suggestive of local solute depletion phenomena, causing multiple simultaneous oxidation reactions to occur and transition to other oxides as specific constituents are selectively oxidized and consumed [29]. Near the oxide-IRZ interface, the scale is primarily tantalum-rich (Fig. 11(b)), with titanium-rich (Fig. 11(c)) bands streaking out from the dark precipitates in the metal substrate. Small, discontinuous chromium-rich (Fig. 11(d)) regions are dispersed throughout the scale. EDS measurements on location 4 revealed that the titanium-rich regions are TiO_2, further confirming the XRD observations (Fig. 11(a), Table 5). There is a distinct region of oxygen-enrichment (Fig. 11(e)) in the oxide scale directly below the nitrogen-rich layer (Fig. 11(f)). Region 5 was measured to be TiN. The dark precipitates in the IRZ (Fig. 11(b), location 7) are titanium-rich and are likely oxygen-stabilized *hcp*, exhibiting morphological similarity to α-Ti precipitate structures present in many β-Ti alloys, e.g. Ti-5Al-5Mo-5V-3Cr (Ti-5553) [31,34,35]. Small Laves precipitates were seen along the grain boundary *hcp* precipitates (Fig. 11(b), location 8, Table 5). Within the IRZ, the *bcc* matrix remained tantalum-rich; however, the titanium content was depleted in comparison to the pre-test composition.

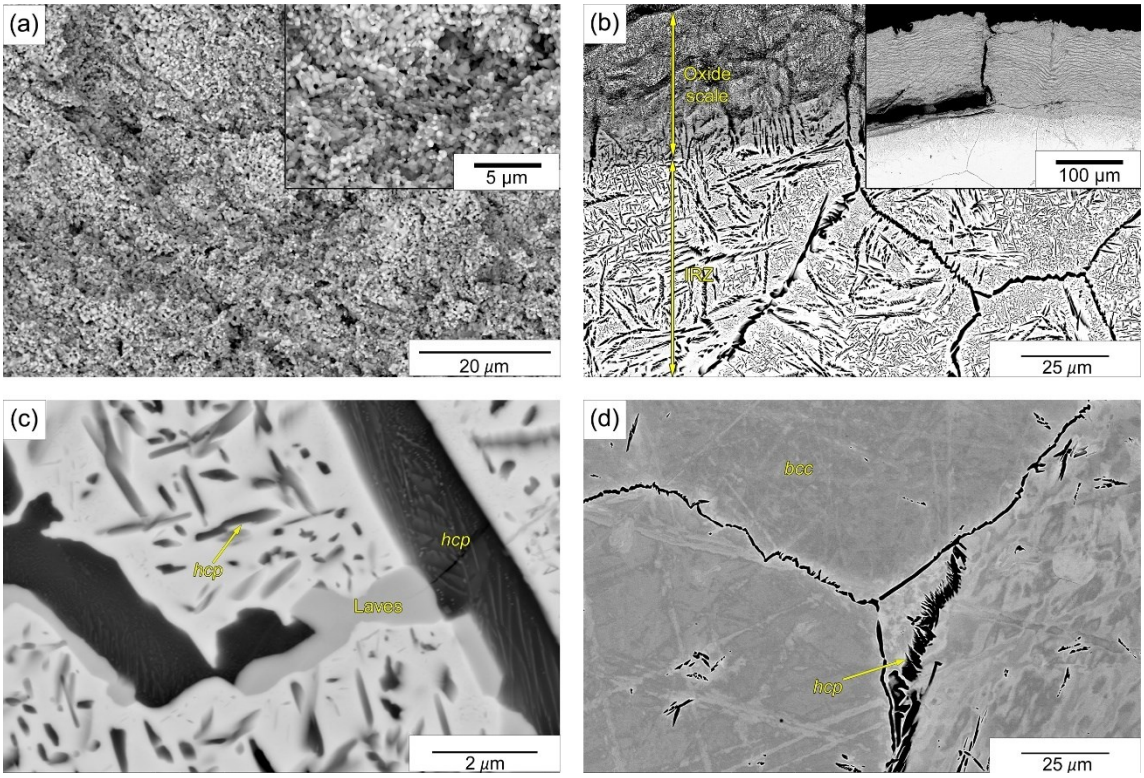

Figure 10. Backscatter SEM micrographs of the Ta_4Ti_3Cr sample after the oxidation test (24 hours at 1200°C in air). (a) Free surface of oxide scale showing TiO_2, (b) cross-section showing IRZ and (inset) oxide scale after 1-hour oxidation test, (c) needle-like particles near coarse grain boundary precipitates, and (d) reacted center of the sample showing grain boundary precipitation.

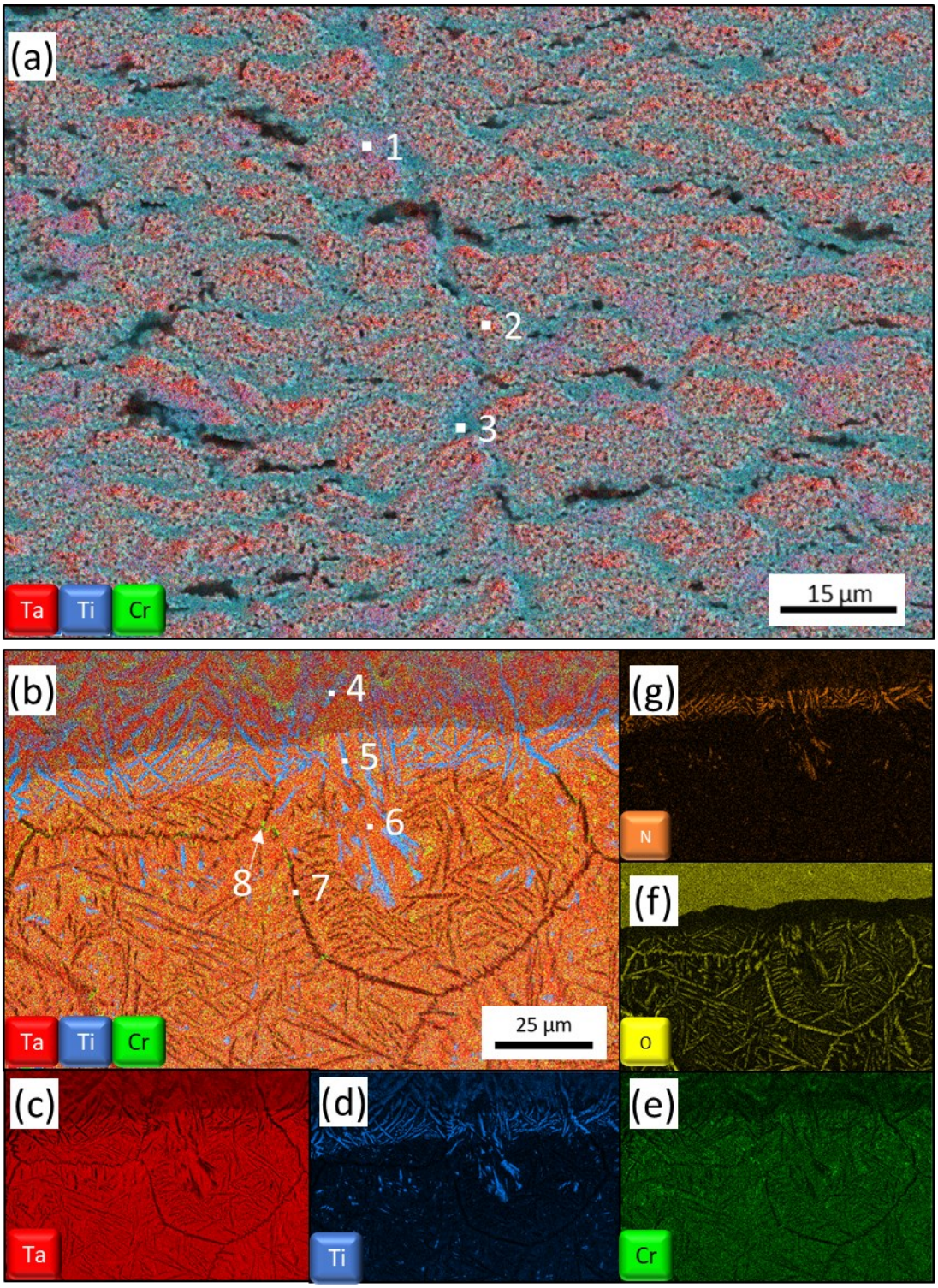

Figure 11. EDS maps of the Ta_4Ti_3Cr alloy after 24 hrs of oxidation at 1200°C, showing a composite map of the (a) oxide scale, (b) IRZ, (c) tantalum, (d) titanium, (e) chromium, (f) oxygen, (g) nitrogen content in the alloy.

Table 5. EDS measurements for the observed phases in the Ta_4Ti_3Cr alloy after oxidation at 1200 °C for 24 hrs.

Region	Fig., location	Phase	Cr	Ta	Ti	O	N
Free Surface	**10(a)**	TiO_2	4.51	4.86	18.23	72.4	-
External Oxides	**11,1**	Ta_2TiO_7	0.1	18.7	10.9	69.6	
	11,2	Ta_2O_5	1.1	23.4	4.5	70.5	-
	11,3	$(Cr,Ta,Ti)_2O_4$	7.9	6.5	18.7	66.9	
	11,4	TiO_2	3.3	6.3	23.2	67.2	
IRZ	**11,5**	TiN	2.5	3.5	41.4	-	52.6
	11,6	*bcc*	8.6	62.9	20.5	8.0	-
	11,7	*hcp*	2.0	3.9	67.8	23.4	3.0
	11,8	Laves	53.0	35.5	11.5	-	-

3.3.3 Ta_2TiCr Post-Oxidation

Consistent with the other alloys, TiO_2 was the primary oxide observed on the free surface of the Ta_2TiCr specimen (Fig. 12(a)), along with $CrTaO_4$ clusters dispersed throughout. The Ta_2TiCr alloy formed a thick, porous scale with a thickness of 1.15mm, showing a measurable separation from the metal-oxide interface (Fig. 12(b)) after 13 hours. The IRZ (Fig. 12(b)) was approximately 150µm thick and was morphologically similar to the starting microstructure (Fig. 3(e)), with the addition of a dark precipitate phase that formed along the primary and secondary Laves phase boundaries, as well as fine, acicular precipitates that grew in the *bcc* matrix (Fig. 12(c)). The unreacted center of the specimen (Fig. 12(d)) remained *bcc* + Laves, with some coalescence and growth of the primary Laves and dissolution of secondary Laves, due to the high temperature exposure.

Figure 13(a) shows a composite EDS map of the Ta_2TiCr oxide scale after a 13-hour oxidation test. The external oxide scale consisted of a periodic layered structure of similar morphology to the Ta_4Ti_3Cr alloy. The repeating structure shown in Fig. 13(a), location 1 was measured to be $(Cr,Ta,Ti)_2O_4$, with Ta_2O_5 pockets (Fig. 13(a), location 2) surrounded by regions of $TaTiO_4$ (Fig. 13(a), location 3, Table 6). Near the oxide-IRZ interface (Fig. 13(b)), the scale was mostly tantalum-rich (Fig. 13(c)), with layers of titanium enrichment (Fig. 13(d)) and chromium enrichment (Fig. 13(e)). Unlike the previous alloys, oxygen remained almost exclusively in the external scale (Fig. 13(f)). At the metal-oxide interface there is a slightly nitrogen -rich region with small, titanium -rich particles dispersed throughout (Fig. 13(g)), confirmed by EDS to be TiN (Fig. 13(b), location 4). Figure 13(b), locations 5 and 6 show Laves and *bcc*, respectively. Deeper into the IRZ, small Ti-rich precipitates were present within the matrix. These particles have chemistry consistent with *hcp* titanium (Fig. 13(b), location 7, Table 6). Below the nitrogen -rich region, a titanium -depleted zone can be seen (Fig 13(d)).

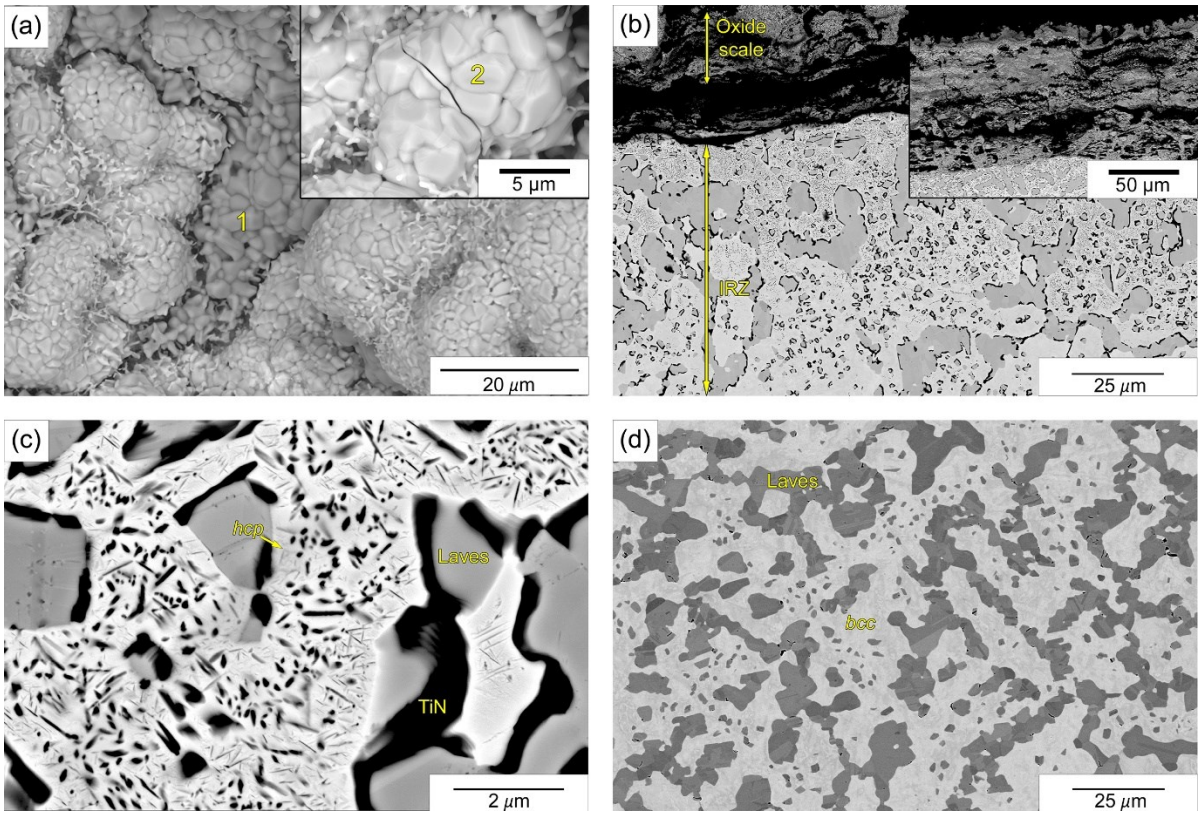

Figure 12. Backscatter SEM micrographs of the Ta_2TiCr sample after the oxidation test (13 hours at 1200°C in air). (a) Free surface of oxide scale showing (1) TiO_2 and (2) $CrTaO_4$, (b) cross-section showing IRZ and (inset) oxide scale after 1-hour oxidation test, (c) fine matrix and grain boundary precipitates, and (d) unreacted center of the sample.

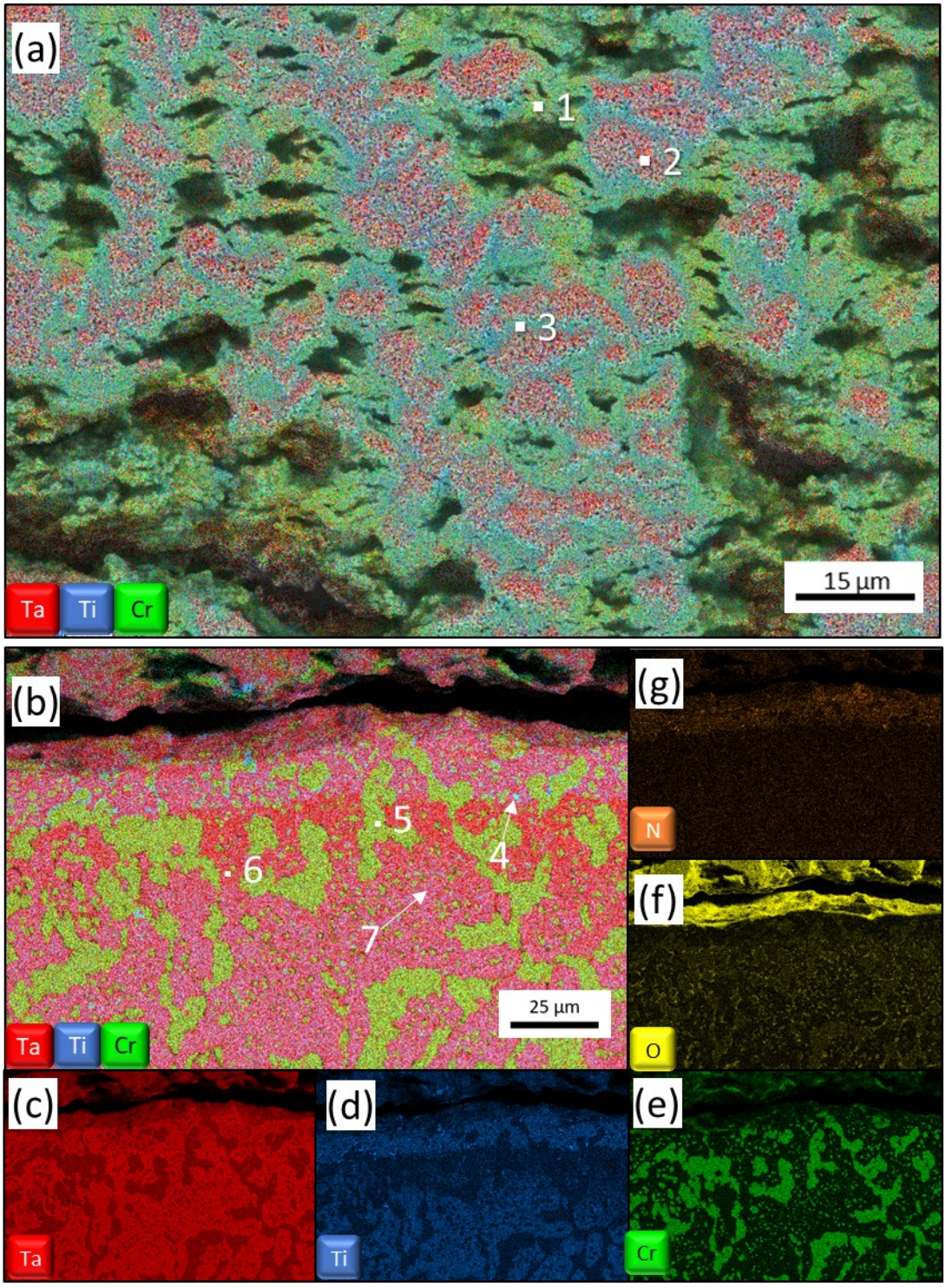

Figure 13. Post-oxidation EDS maps of the Ta_2TiCr alloy after 13 hrs of oxidation at 1200°C, showing a composite map of the (a) oxide scale, (b) IRZ, (c) tantalum, (d) titanium, (e) chromium, (f) oxygen, (g) nitrogen content in the alloy.

Table 6. EDS measurements for the observed phases in the Ta_2TiCr alloy after oxidation at 1200°C for 13 hrs

Region	Fig., location	Phase	Cr	Ta	Ti	O	N
Free Surface	**12(a), 1**	TiO_2	0	1.4	43.8	54.8	-
	12(a), 2	$CrTaO_4$	13.2	18.3	2.4	66.1	-
External Oxides	**13, 1**	$(Cr,Ta,Ti)_2O_4$	9.2	9.8	11.4	69.6	-
	13, 2	Ta_2O_5	0.6	23.7	0.5	75.3	-
	13, 3	$TaTiO_4$	5.5	11.3	15.5	67.6	-
IRZ	**13, 4**	Laves	53.0	29.4	17.6	-	-
	13, 5	TiN	2.1	10.9	53.6	4.4	29.0
	13, 6	*bcc*	9.7	62.5	22.4	5.3	-
	13, 7	*hcp*	2.0	8.2	70.6	19.2	-

3.3.4 Ta_4TiCr_3 Post-Oxidation

Unlike the other alloys, the free surface of the Ta_4TiCr_3 oxide scale was entirely Cr_2O_3 (Fig. 14(a), inset). The wavy, coral-like morphology of the free surface (Fig. 14(a)) is likely the result of oxide rumpling, which is generally caused by growth stresses during oxidation testing [36]. Rumpling is also likely exacerbated by the expected volatilization of Cr_2O_3 at 1200°C [29,37]. The cross-section of the Ta_4TiCr_3 alloy shows the formation of a thick, porous scale, similar to Ta_2TiCr, that lost adhesion with the metal-oxide interface (Fig. 14(b)) after 24 hours. The scale was measured to be 600µm thick on average. The IRZ (Fig 14(b)) was approximately 100µm thick and had similar features as Ta_2TiCr, with dark precipitate phases that formed along primary and secondary Laves phase boundaries. Dark, globular precipitates were also seen in the matrix. Similar to the oxidized TaTiCr alloy, dark, needle-like precipitates were also seen in the Laves particles along with noticeable cracking (Fig. 14(c)). The unreacted center (Fig. 14(d)) of the specimen remained *bcc* + Laves, with an increased phase fraction of secondary Laves precipitates after oxidation (0.055 → 0.078).

The surface of the oxide scale (Fig. 15(a)) consisted of a layered structure, with a Cr_2O_3 outer layer (Fig. 15(a), location 1), a $CrTaO_4$ middle layer (Fig. 15(a), location 2), and large Ta_2O_5 structures (Fig. 15(a), location 3) above a layer of $(Cr,Ta,Ti)_2O_4$ (Fig. 15(a), location 4). This section was separated from the bulk oxide (Fig. 15(b)), likely due to the rumpling effects and oxide growth. The bulk oxide scale again consisted of a periodic layered structure (Fig. 15(b)) that had similar oxide structures as the surface (Fig. 15(a)) but with very different morphologies. The majority of the scale consisted of $CrTaO_4$ (Fig. 15(b), location 2), with Ta_2O_5 pockets (Fig. 15(b), location 3) surrounded by small areas of $(Cr,Ta,Ti)_2O_4$ (Fig. 15(b), location 4). Thin bands of Cr_2O_3 were seen (Fig. 15(b), location 1), indicating the periodicity of the scale. Near the surface (Fig. 15(c)), the scale was mostly tantalum -rich (Fig. 15(d)), with layers of chromium -enrichment (Fig. 15(f)); while titanium (Fig. 15(e)) was only observed as precipitates in the IRZ. The discontinuous chromium -rich regions had a chemistry consistent with Cr_2O_3 (Table 7). The fine, dark globular precipitates in the matrix are likely *hcp* however further work is needed to fully characterize these very small features. The titanium -rich dark precipitates surrounding the Laves particles were measured to be TiO_2 (Fig. 15(c), location 5), differing from the other alloys. Figure 15(c) also shows the presence of *bcc* (Fig. 15(c), location 6) and Laves (Fig. 15(c), location 7). Similar to the

Ta_2TiCr alloy, there was minimal oxygen (Fig. 15(g)) retention in the metal, and very small dispersions of nitrogen (Fig. 15(h)) near the metal-oxide interface.

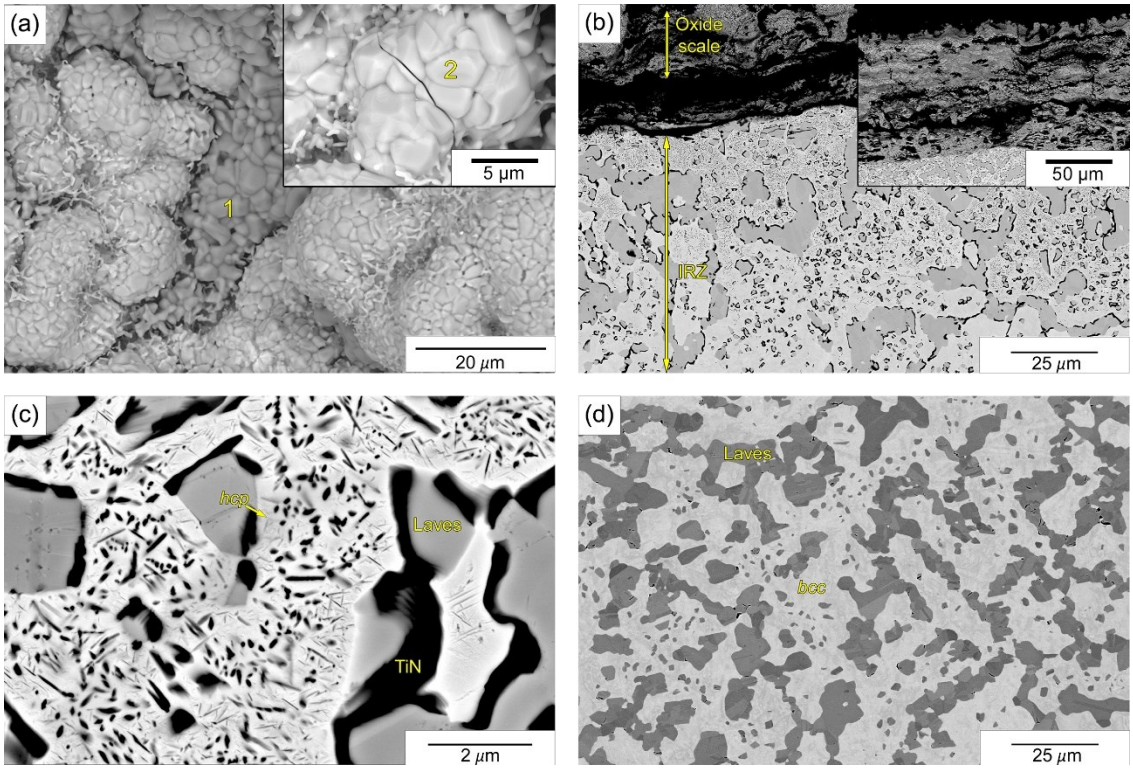

Figure 14. Backscatter SEM micrographs of the Ta_4TiCr_3 sample after the oxidation test (24 hours at 1200°C in air). (a) Free surface of oxide scale showing rumpled Cr_2O_3 scale, (b) cross-section showing IRZ and (inset) oxide scale after 1-hour oxidation test, (c) titanium nucleation in bcc *matrix and cracked Laves particles, and (d) unreacted center of the sample.*

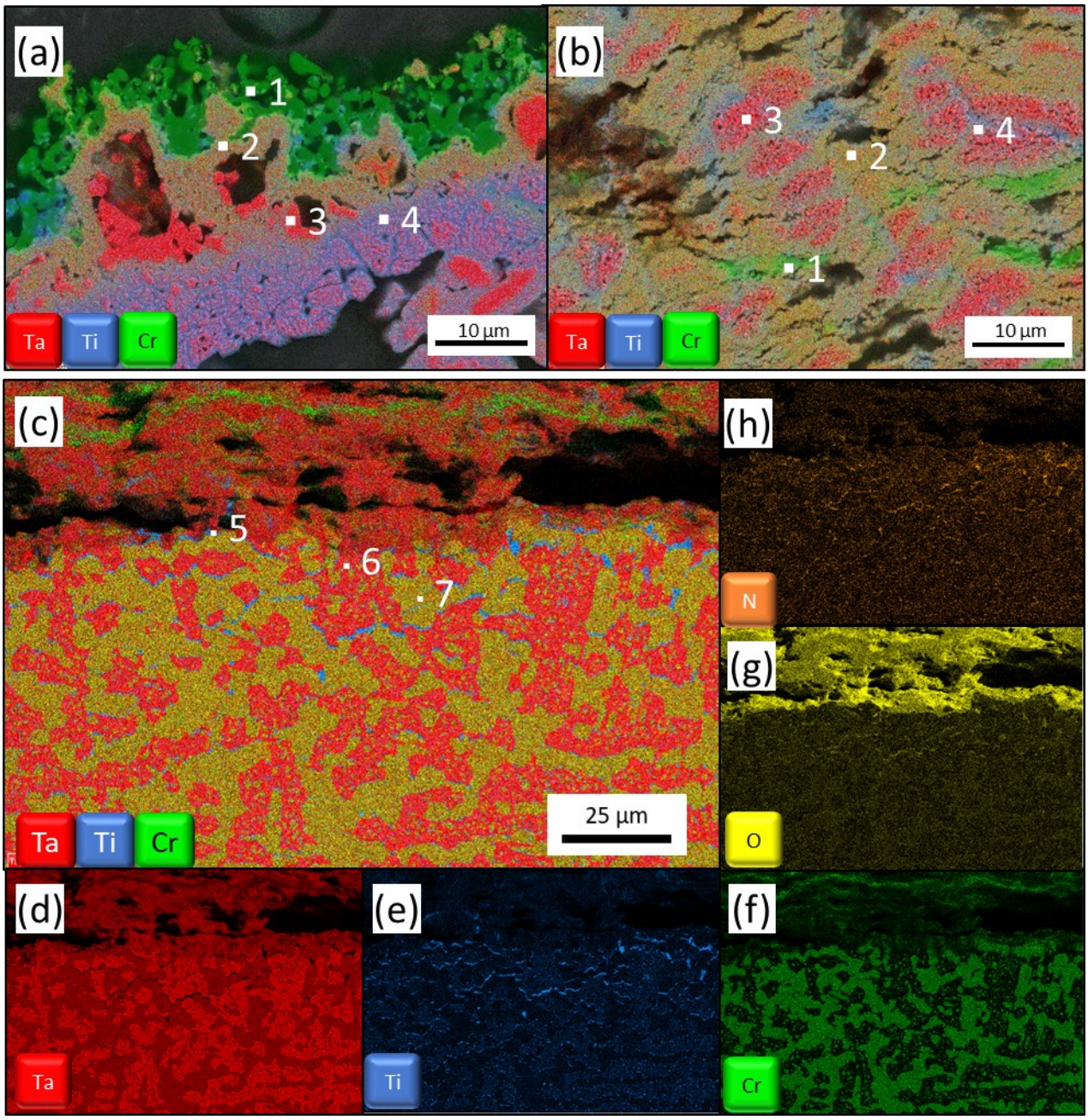

Figure 15. Post oxidation EDS maps of the Ta_4TiCr_3 alloy after 24 hrs of oxidation at 1200°C, showing a composite map of the (a) surface oxide scale, (b) bulk oxide scale, (c) IRZ, (d) Ta, (e) Ti, (f) Cr, (g) O, (h) N content in the alloy.

Table 7. EDS measurements for the observed phases in the Ta_4TiCr_3 alloy after oxidation at 1200°C for 24 hrs

Region	Fig., location	Phase	Cr	Ta	Ti	O	N
Free Surface	**14(a)**	Cr_2O_3	34.95	0.72	1.7	62.63	-
External Oxides	**15,1**	Cr_2O_3	38.1	0.3	1.3	60.3	-
	15,2	$CrTaO_4$	14.9	15.3	3.2	66.7	-
	15,3	Ta_2O_5	0.4	28.3	-	71.3	-
	15,4	$(Cr,Ta,Ti)_2O_4$	10.2	13.0	9.6	67.1	-
IRZ	**15,5**	TiO_2	5.3	7.7	45.7	41.3	-
	15,6	*bcc*	5.1	64.6	10.6	-	19.7
	15,7	Laves	62.9	34.8	2.3	-	-

4. Discussion

4.1 Influence of composition on microstructure and oxide products

All alloys analyzed in this work formed microstructures including *bcc* + Laves (TaTiCr, Ta_2TiCr, and Ta_4TiCr_3) or single-phase *bcc* (Ta_4Ti_3Cr). The effect of elemental concentration on the microstructure constitution and morphology can be clearly seen throughout this paper, as increasing the overall Cr content leads to higher Laves phase fractions. The transition from discontinuous Laves particle morphology of alloys with 25-33 at% Cr (0.34-0.49 phase fraction, respectively) to continuous Laves morphology of the alloy with the highest chromium concentration of 37.5 at% Cr (0.51 phase fraction) (Fig. 3) was observed. Interestingly, the Laves phase composition and the chromium content in the *bcc* matrix both remain relatively constant between alloys (Table 2) while the matrix composition varies greatly with the respective Ta:Ti composition ratios (Fig. 16). The TaTiCr alloy exhibited a highly titanium-rich matrix; the Ta_4Ti_3Cr alloy has a tantalum-rich matrix, which likely deviates from the trend due to the lack of predicted Laves phase formation, which would absorb a moderate amount of tantalum; the Ta_2TiCr alloy has a slightly tantalum-rich matrix; and the Ta_4TiCr_3 alloy has a highly tantalum-rich matrix (Fig. 16). The matrix phase compositions and Laves morphologies appear to greatly influence oxidation and nitridation products and morphologies.

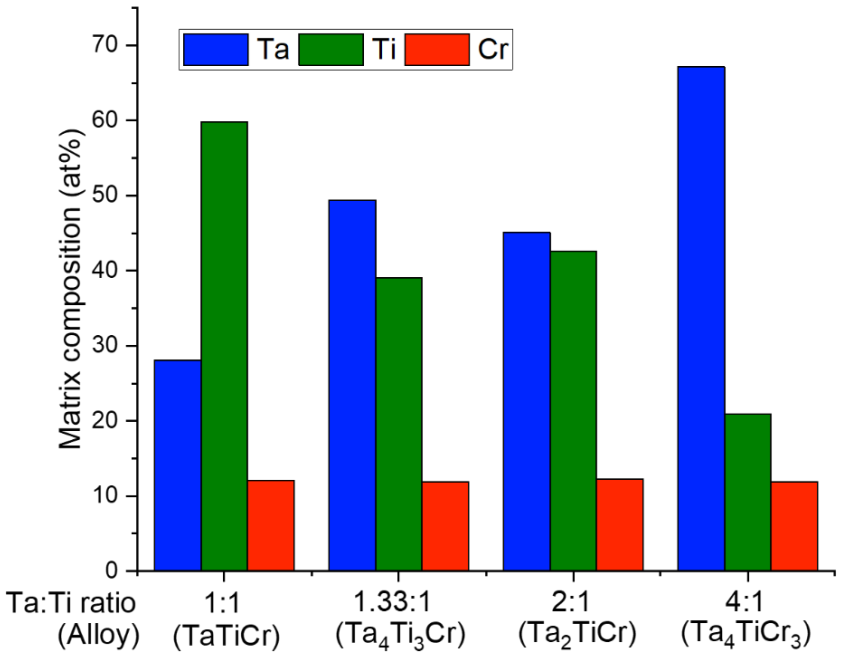

Figure 16: Matrix composition (at%) compared to respective Ta:Ti alloying ratio in each alloy.

In general, as the titanium content in the matrix increases, the coarser the TiN precipitates appear in the IRZ after oxidation, manifesting as large, lenticular precipitates in the TaTiCr alloy (Fig. 3(b)), and smaller, dispersed precipitates in the Ta_2TiCr (Fig. 12(b)) and the Ta_4Ti_3Cr (Fig. 10(b)) alloys. The Ta_4TiCr_3 alloy had the lowest titanium matrix composition (20.9 at%) and did not produce any TiN in the IRZ (Fig. 14(b)).

The elemental concentration influences oxide product formation. All alloys except the titanium-lean Ta_4TiCr_3 alloy showed a surface layer of TiO_2 on the oxide scale and the chromium -rich alloys (TaTiCr and Ta_4TiCr_3) exhibited a preferable tendency to form Cr_2O_3. Mixed rutile structures appeared in all alloys, as expected from the chosen alloy space explored in this work. The Ta_2O_5 oxide only appeared in the external oxide scale of the alloys containing 50 at% Ta (Ta_4Ti_3Cr, Ta_2TiCr, and Ta_4TiCr_3); however, a small layer was seen at the oxide-IRZ interface in the TaTiCr alloy. The relative similarity in oxide products between the alloys in comparison to the large difference in oxidation performance suggests that oxide morphology is highly influential in oxidation behavior for these alloys.

4.2 Oxidation kinetics and oxide morphologies

The oxidation behavior of the TaTiCr, Ta_4Ti_3Cr, Ta_2TiCr, and Ta_4TiCr_3 alloys was significantly different, pointing to the large influence of composition on the resulting microstructures and oxidation performance of alloys in this system. The Ta_2TiCr alloy performed the poorest, since it completely oxidized after 24 hours. Interestingly, this alloy did not form any protective Cr_2O_3 and instead formed $(Cr,Ta,Ti)_2O_4$ and $CrTaO_4$ oxides. Although $CrTaO_4$ has been reported to be highly protective as a continuous, adherent scale [5,12,14,23], evidence showed that the discontinuous morphology of the oxide in the Ta_2TiCr alloy offered very little protection. Additionally, the periodic oxide structure contained large amounts of the deleterious Ta_2O_5. The discontinuous TiN precipitates in the IRZ provided little protection within the Ta_2TiCr alloy to halt oxygen ingress and therefore interface-controlled

internal oxidation became the dominant mechanism early on, corroborated by the near-linear oxidation kinetics (n =1.03) observed during the oxidation test. While the Ta_4Ti_3Cr alloy did not form any protective oxides, the through-thickness grain boundary *hcp* precipitation may have aided in slowing the internal oxidation front by increasing tortuosity for diffusion near precipitates. Additionally, the *hcp* phase acts as an O sink or "getter", leading to selective oxide formation and consumption by reaction instead of following interface-controlled diffusion kinetics [29]. The intermediate kinetics (n = 0.83) support the proposed oxidation mechanism by rationalizing the suggested mixed diffusion-controlled and interface-controlled oxidation modes. Similar to the Ta_2TiCr alloy, the Ta_4Ti_3Cr alloy did not form any protective oxides and exhibited extensive internal oxidation.

The Ta_4TiCr_3 alloy experienced multiple oxidation kinetic regimes during the 24-hour test. Unlike the other four alloys that formed rutile TiO_2 in the outer scale layers, the Ta_4TiCr_3 alloy first grew a protective Cr_2O_3 scale, responsible for the initial parabolic kinetics (n = 0.51) during the test due to diffusion-limited growth. The continuous Laves phase may have provided protection by increasing tortuosity of the oxygen diffusion path, in a similar manner as the lenticular TiN precipitates in the TaTiCr alloy. Cr_2O_3 volatilization was likely occurring for the entire test and, in conjunction with growth stresses, resulted in the rumpled, wavy, coral-like surface scale (Fig. 14(a)). When tantalum oxidizes and forms Ta_2O_5, a large volumetric change occurs (Pilling-Bedworth Ratio = 2.47) [38]. The presence of large Ta_2O_5 structures beneath the outer scale in the Ta_4TiCr_3 alloy is likely the main contributor to the onset of the rumpling by deforming the Cr_2O_3 scale during oxidation [29]. The onset of rumpling creates voids between the Cr_2O_3 scale and the surface of the Ta_4TiCr_3 alloy, initiating the growth of the discontinuous repeating oxide structure of $(Cr,Ta,Ti)_2O_4$ and Ta_2O_5, marking the onset of the second, linear regime(n = 1.17). As the periodic structure continued to grow, the growth stresses and volatilization may have accumulated until the rumpled scale developed cracks and offered little to no protection, resulting in a rapid internal oxidation regime until the end of the test (n = 3.19).

Finally, the TaTiCr alloy exhibited the best performance by a sizable margin. Although the oxide scale contained similar mixed rutile structures like the other alloys, the scale morphology was continuous, adherent, and compact, leading to a higher degree of protection. Interestingly, the protective $CrTaO_4$ oxide reported elsewhere [5,22] was not seen in the oxide scale, suggesting the cascading rutile oxide layer ($CrTiO_4$, $(Cr,Ta,Ti)_2O_4$, and $TaTiO_4$) provided a similar level of protection. Recently, Schellert, et al. [39] investigated the $(Cr,Ta,Ti)_2O_4$ (designated as $(Cr,Ta,Ti)O_2$) in the Ta-Mo-Cr-Ti-Al system and reported the nonstoichiometric chemical nature of the oxide through Electron Energy Loss Spectroscopy (EELS). The oxide was reported to reduce oxygen ingress by means of cation and have a high thermodynamic stability, aiding in oxidation performance. As previously stated, this oxide also aids in oxidation performance in the TaTiCr alloy when present in a continuous, compact scale. The semi-continuous lenticular TiN particles in the TaTiCr alloy are likely acting as obstacles to oxygen ingress into the specimen, due to the tortuous diffusion path imposed by the TiN morphology. The IRZ morphology of the TaTiCr alloy may have aided in the growth of a continuous Cr_2O_3 scale, as this was the only specimen with an adherent Cr_2O_3 layer after 24 hours Additionally, the Laves particles near the surface functioned as chromium reservoirs and provided cations to form the Cr_2O_3 scale, evident by the complete depletion of Cr in the prior-Laves particles after oxidation.

4.3 Performance of related alloys

Comparing the studied the Ta-Ti-Cr alloys to other related RCAs, many similarities can be seen in both phases and oxide products. There are, however, large differences in performance between the various alloys (Table 8), suggesting morphological effects greatly influence the oxidation behavior, as previously discussed.

The general trends show that Al_2O_3- and Cr_2O_3-forming alloys exhibit excellent oxidation resistance; vice versa, Ta_2O_5-structured oxides (Ta_2O_5 and $(Nb,Ta)_{10}O_{25}$) tend to have adverse effects on oxidation performance. Brady et al. [14] reports that the Cr-10Ta alloy had a near-eutectic microstructure consisting of *bcc* chromium and globular Cr_2Ta Laves with excellent oxidation resistance over the course of 120 hours by forming a scale consisting of an outer Cr_2O_3 scale and an inner, compact $CrTaO_4$ layer, and an IRZ of mixed Cr-Ta nitrides and metallic *bcc* Cr. The alloy most similar to the TaTiCr alloy, in terms of general morphology and oxide products, is the CrNbTi alloy reported by Butler et al. [3], with a nearly identical IRZ to the TaTiCr alloys with coarse lenticular TiN dispersed between Laves particles. Additionally, the CrNbTi alloy contained a compact multi-layered scale of an outer TiO_2 layer, an intermediate Cr_2O_3 layer, and an inner $NbTiO_4$ layer. Furthermore, Butler et al. [3] stated that the CrNbTaTi alloy had a starting microstructure whose morphology was quite similar to the Ta_2TiCr alloy and, similarly formed a thick, periodic oxide scale containing mixed rutile and Ta_2O_5-structured oxide products. The IRZ for the CrNbTaTi alloy contained coarser TiN particles which likely explains the heightened performance compared to the Ta_2TiCr alloy, which was completely oxidized after testing. The TaMoCrTiAl [21] alloy performed slightly better in oxidation tests than the TaTiCr alloy at the same temperature and duration. In addition to Cr_2O_3, $CrTaO_4$ and TiO_2, the compact oxide scale contained a protective Al_2O_3 external oxide layer and an IRZ consisting of lenticular TiN and Al_2O_3. The common material characteristic between the superior performers amongst these alloys at temperatures >1000 °C (TaTiCr, Cr-10Ta, CrNbTi, and TaMoCrTiAl) is the internal reacted zone that consists of semi-continuous corrosion products (TiN, (Cr,Ta)N, and Al_2O_3), further supporting the hypothesis that these products aid in reducing oxygen ingress and provide a framework for protective, compact external oxides.

Table 8: Oxidation behaviors of concentrated refractory alloys related to the Ta-Ti-Cr system.

Alloy	**Condition**	**Phases**	**T,°C**	**Time, h**	**Δm, mg/cm^2**	**Oxide Products**
TaTiCr	HIP	*bcc*/Laves	1200	24	7.1	Cr_2O_3, $CrTiO_4$, $(Cr,Ta,Ti)_2O_4$, Ta_2O_5, $TaTiO_4$, TiO_2
Ta_4Ti_3Cr	HIP	*bcc*	1200	24	124.1	$(Cr,Ta,Ti)_2O_4$, Ta_2O_5 $TaTiO_4$, Ta_2TiO_7, TiO_2
Ta_2TiCr	HIP	*bcc*/Laves	1200	24	160.9	$CrTaO_4$, $(Cr,Ta,Ti)_2O_4$, Ta_2O_5 $TaTiO_4$, TiO_2
Ta_4TiCr_3	HIP	*bcc*/Laves	1200	24	71.5	Cr_2O_3, $CrTaO_4$, $(Cr,Ta,Ti)_2O_4$, Ta_2O_5
Cr-10Ta [14]	HIP	*bcc*/Laves	1100	120	8	Cr_2O_3, $CrTaO_4$
CrNbTi [3]	HIP	*bcc*/Laves	1200	24	19.2	Cr_2O_3, $NbTiO_4$, TiO_2
CrNbTaTi [3]	HIP	*bcc*/Laves	1200	24	61.9	Cr_2O_3, Cr_2TiO_5, $(Cr,Ta,Ti)_2O_4$,$(Nb,Ta)_{10}O_{25}$, $TaTiO_4$
TaMoCrTiAl [21]	Annealed	*bcc*/B2/Laves	1200	24	5	Al_2O_3, Cr_2O_3, $CrTaO_4$, TiO_2

5. Conclusions

The oxidation behaviors of the TaTiCr, Ta_4Ti_3Cr, Ta_2TiCr, and Ta_4TiCr_3 alloys at 1200°C were explored in this work. The ternary TaTiCr alloy test results showed far superior oxidation performance than the other three alloys, suggesting that microstructure morphology and phase composition play an important role on the oxidation behavior for this system. The following key points can be made from the discussed results:

- The Ta-Ti-Cr system consists of a *bcc* matrix and C15 Laves precipitates. The matrix was titanium-rich in the TaTiCr alloy and tantalum-rich in the Ta_4Ti_3Cr, Ta_2TiCr, and Ta_4TiCr_3 alloys. The relative Laves phase fraction is proportional to the chromium content in the alloy, with the Ta_4Ti_3Cr (Cr = 12.5 at%) alloy exhibiting no Laves after HIP, and the Ta_4TiCr_3 (Cr = 37.5 at%) alloy having a Laves phase fraction of 0.52. The Laves morphology was discontinuous and dispersed in the alloys containing 25% Cr (Ta_2TiCr) and 33% Cr (TaTiCr) and was continuous in the alloy containing 37.5% Cr (Ta_4TiCr_3).
- The Laves phase compositions and chromium content in the *bcc* matrix remained relatively constant for each alloy; however, the tantalum and titanium content in the matrix varied with respect to the Ta:Ti ratio in each alloy. The titanium matrix composition influenced the TiN morphology in the IRZ, with the TaTiCr alloy having coarse, semi-continuous TiN precipitates and all other alloys having fine, discontinuous precipitates. The TiN and Laves morphology directly influenced the oxide scale morphology, manifesting as a compact, multi-layered scale in the TaTiCr alloy and periodic, porous scales in the other alloys.
- The TaTiCr alloy had the slowest kinetics, exhibiting near-cubic kinetic behavior for the entire 24-hour test. The Ta_4TiCr_3 alloy was the second-best performer, showing three distinct regimes: a near-parabolic regime from 0-9 hours, a linear regime from 9-16 hours, and a higher-rate linear regime from 16-24 hours. These three regimes are attributed to oxide rumpling, cracking, and subsequent internal oxidation. The Ta_2TiCr and Ta_4Ti_3Cr alloys both displayed near-linear kinetics for the duration of the 24-hour test forming thick, porous oxides that showed severe cracking. The Ta_2TiCr alloy was completely oxidized after 24 hours.
- After 24 hours at 1200°C the TaTiCr alloy formed a coherent, layered oxide scale consisting of an outer layer of TiO_2, followed by Cr_2O_3, and mixed rutile-structured oxides. The IRZ was highly complex and contained Ta_2O_5 at the oxide-IRZ interface in addition to a remnant tantalum-rich *bcc* matrix with semi-continuous TiN and Laves particles with superfine acicular titanium precipitates. The Ta_4TiCr_3 alloy formed a moderately thick scale with an outer layer of Cr_2O_3 with a high degree of rumpling. Beneath the outer Cr_2O_3 layer, the scale consisted of repeating structures similar to the Ta_4Ti_3Cr and the Ta_2TiCr alloys consisting of discontinuous Cr_2O_3, Ta_2O_5, and mixed rutile oxides. The IRZ of the Ta_4TiCr_3 alloy contained fine titanium-rich precipitates both in the matrix and within the Laves phase, and TiO_2 precipitates on the Laves phase boundaries. The Ta_4Ti_3Cr and the Ta_2TiCr alloys both formed complex, discontinuous, repeating oxide scales that consisted of Ta_2O_5, Ta_2TiO_7, and mixed rutile oxides; however, the IRZs for both alloys were very different. The Ta_4Ti_3Cr alloy IRZ wove through the entire specimen and consisted of a remnant *bcc* matrix with fine TiN particles near the metal-oxide interface, coarse *hcp* precipitates at grain boundaries, and fine needle-like *hcp* precipitates within grains. The Ta_2TiCr alloy IRZ was similar to the Ta_4TiCr_3 alloy, with fine *hcp* precipitates and TiN particles in the matrix.

CRediT authorship contribution statement

Noah J. Welch: Conceptualization, Methodology, Investigation, Data Curation, Writing - Original Draft, Writing - Review & Editing, Visualization. **Maria J. Quintana:** Conceptualization, Methodology, Data Curation, Writing - Original Draft, Writing - Review & Editing, Visualization. **Todd M. Butler:** Conceptualization, Methodology, Writing - Review & Editing, Supervision. **Peter C. Collins:** Conceptualization, Methodology, Writing - Review & Editing, Supervision.

Declaration of Competing Interest

The authors declare that they have no known competing financial interests or personal relationships that could have appeared to influence the work reported in this paper.

Acknowledgements

The authors acknowledge the support of the Center for Advanced Non-Ferrous Structural Alloys (CANFSA), an NSF Industry/University Cooperative Research Center (I/UCRC) between Iowa State University and The Colorado School of Mines under NSF-IIP award #1624748. The views, opinions and/or findings expressed are those of the author and should not be interpreted as representing the official views or policies of the Department of Defense or the U.S. Government.

References

[1] N.R. Philips, M. Carl, N.J. Cunningham, New Opportunities in Refractory Alloys, Metallurgical and Materials Transactions A. 51 (2020) 3299–3310. https://doi.org/10.1007/s11661-020-05803-3.

[2] O.N. Senkov, D.B. Miracle, K.J. Chaput, J.-P. Couzinie, Development and exploration of refractory high entropy alloys—A review, J Mater Res. 33 (2018) 3092–3128. https://doi.org/10.1557/jmr.2018.153.

[3] T.M. Butler, O.N. Senkov, T.I. Daboiku, M.A. Velez, H.E. Schroader, L.G. Ware, M.S. Titus, Oxidation behaviors of CrNb, CrNbTi, and CrNbTaTi concentrated refractory alloys, Intermetallics (Barking). 140 (2022). https://doi.org/10.1016/j.intermet.2021.107374.

[4] O. Kubaschewski, B.E. Hopkins, Oxidation mechanisms of niobium, tantalum, molybdenum and tungsten, Journal of the Less Common Metals. 2 (1960) 172–180. https://doi.org/https://doi.org/10.1016/0022-5088(60)90012-6.

[5] S. Schellert, B. Gorr, S. Laube, A. Kauffmann, M. Heilmaier, H.J. Christ, Oxidation mechanism of refractory high entropy alloys Ta-Mo-Cr-Ti-Al with varying Ta content, Corros Sci. 192 (2021). https://doi.org/10.1016/j.corsci.2021.109861.

[6] J. Chen, X. Zhou, W. Wang, B. Liu, Y. Lv, W. Yang, D. Xu, Y. Liu, A review on fundamental of high entropy alloys with promising high–temperature properties, J Alloys Compd. 760 (2018) 15–30. https://doi.org/https://doi.org/10.1016/j.jallcom.2018.05.067.

[7] O.N. Senkov, G.B. Wilks, D.B. Miracle, C.P. Chuang, P.K. Liaw, Refractory high-entropy alloys, Intermetallics (Barking). 18 (2010) 1758–1765. https://doi.org/https://doi.org/10.1016/j.intermet.2010.05.014.

[8] T.M. Butler, High Entropy Alloys: Oxidation, in: F.G. Caballero (Ed.), Encyclopedia of Materials: Metals and Alloys, Elsevier, Oxford, 2022: pp. 522–532. https://doi.org/https://doi.org/10.1016/B978-0-12-803581-8.12126-5.

[9] O.N. Senkov, S. Gorsse, D.B. Miracle, High temperature strength of refractory complex concentrated alloys, Acta Mater. 175 (2019) 394–405. https://doi.org/https://doi.org/10.1016/j.actamat.2019.06.032.

[10] T.M. Butler, O.N. Senkov, M.A. Velez, T.I. Daboiku, Microstructures and mechanical properties of CrNb, CrNbTi, and CrNbTaTi concentrated refractory alloys, Intermetallics (Barking). 138 (2021). https://doi.org/10.1016/j.intermet.2021.107323.

[11] A. Bhowmik, H.T. Pang, I.M. Edmonds, C.M.F. Rae, H.J. Stone, Effect of silicon additions on the high temperature oxidation behaviour of Cr–Cr2Ta alloys, Intermetallics (Barking). 32 (2013) 373–383. https://doi.org/https://doi.org/10.1016/j.intermet.2012.09.013.

[12] M.P. Brady, C.T. Liu, J.H. Zhu, P.F. Tortorelli, L.R. Walker, Effects of Fe additions on the mechanical properties and oxidation behavior of Cr2Ta Laves phase reinforced Cr, Scr

Mater. 52 (2005) 815–819. https://doi.org/https://doi.org/10.1016/j.scriptamat.2005.01.016.

[13] M.P. Brady, P.F. Tortorelli, E.A. Payzant, L.R. Walker, Oxidation Behavior of Cr2N, CrNbN, and CrTaN Phase Mixtures Formed on Nitrided Cr and Laves-Reinforced Cr Alloys, Oxidation of Metals. 61 (2004) 379–401. https://doi.org/10.1023/B:OXID.0000032330.95411.ec.

[14] M.P. Brady, J.H. Zhu, C.T. Liu, P.F. Tortorelli, L.R. Walker, Oxidation resistance and mechanical properties of Laves phase reinforced Cr in-situ composites, Intermetallics (Barking). 8 (2000) 1111–1118. https://doi.org/https://doi.org/10.1016/S0966-9795(00)00046-7.

[15] C.T. Liu, P.F. Tortorelli, J.A. Horton, C.A. Carmichael, Effects of alloy additions on the microstructure and properties of CrCr2Nb alloys, Materials Science and Engineering: A. 214 (1996) 23–32. https://doi.org/https://doi.org/10.1016/0921-5093(96)10197-0.

[16] S. Lu, H. Zheng, L. Deng, J. Yao, Effect of silicon on the fracture toughness and oxidation behavior of hot pressed NbCr2 alloys, Mater Des. 51 (2013) 432–437. https://doi.org/https://doi.org/10.1016/j.matdes.2013.04.033.

[17] H.Z. Zheng, S.Q. Lu, Y. Huang, Influence of grain size on the oxidation behavior of NbCr2 alloys at 950–1200°C, Corros Sci. 51 (2009) 434–438. https://doi.org/https://doi.org/10.1016/j.corsci.2008.11.014.

[18] G.T.J. Mayo, W.H. Shepherd, A.G. Thomas, Oxidation behaviour of niobium-chromium alloys, Journal of the Less Common Metals. 2 (1960) 223–232. https://doi.org/https://doi.org/10.1016/0022-5088(60)90016-3.

[19] R. Smith, The development of oxidation-resistant niobium alloys, Journal of the Less Common Metals. 2 (1960) 191–206. https://doi.org/https://doi.org/10.1016/0022-5088(60)90014-X.

[20] M.P. Brady, B.A. Pint, P.F. Tortorelli, I.G. Wright, R.J. Hanrahan Jr., High-Temperature Oxidation and Corrosion of Intermetallics, in: Materials Science and Technology: A Comprehensive Treatment, John Wiley & Sons, Ltd, 2000: pp. 229–325. https://doi.org/https://doi.org/10.1002/9783527619306.ch15.

[21] B. Gorr, S. Schellert, F. Müller, H.-J. Christ, A. Kauffmann, M. Heilmaier, Current Status of Research on the Oxidation Behavior of Refractory High Entropy Alloys, Adv Eng Mater. 23 (2021) 2001047. https://doi.org/https://doi.org/10.1002/adem.202001047.

[22] S. Schellert, B. Gorr, H. Christ, C. Pritzel, S. Laube, A. Kauffmann, M. Heilmaier, The Effect of Al on the Formation of a CrTaO4 Layer in Refractory High Entropy Alloys Ta-Mo-Cr-Ti-xAl, Oxidation of Metals. 96 (2021). https://doi.org/10.1007/s11085-021-10046-7.

[23] L.-C. Li, M.-X. Li, M. Liu, B.-Y. Sun, C. Wang, J.-T. Huo, W.-H. Wang, Y.-H. Liu, Enhanced oxidation resistance of MoTaTiCrAl high entropy alloys by removal of Al, Sci China Mater. 64 (2021) 223–231. https://doi.org/10.1007/s40843-020-1332-2.

[24] D.E. Huber, Structure and Properties of Titanium Tantalum Alloys for Biocompatibility, 2016. http://rave.ohiolink.edu/etdc/view?acc_num=osu1480589088123473.

[25] A.B. Spierings, M. Schneider, R. Eggenberger, Comparison of density measurement techniques for additive manufactured metallic parts, Rapid Prototyp J. 17 (2011) 380–386. https://doi.org/10.1108/13552541111156504.

[26] T. Moore, P. Moorhead, K. Bowles, Specifications for Cleaning, Fusion Welding, and Postheating Tantalum and Columbium Alloys, Cleveland, 1971.

[27] P.M. Hazzledine, P. Pirouz, Synchroshear transformations in Laves phases, Scripta Metallurgica et Materialia. 28 (1993) 1277–1282. https://doi.org/https://doi.org/10.1016/0956-716X(93)90468-8.

[28] M.F. Chisholm, S. Kumar, P. Hazzledine, Dislocations in Complex Materials, Science (1979). 307 (2005) 701–703. https://doi.org/10.1126/science.1105962.

[29] N. Birks, G.H. Meier, F.S. Pettit, Introduction to the High Temperature Oxidation of Metals, 2nd ed., Cambridge University Press, Cambridge, 2006. https://doi.org/DOI: 10.1017/CBO9781139163903.

[30] G.M. Ecer, G.H. Meier, The effect of Cr2O3 volatilization on the oxidation kinetics of a Ni-Cr alloy, Scripta Metallurgica. 7 (1973) 1189–1194. https://doi.org/https://doi.org/10.1016/0036-9748(73)90245-7.

[31] G. Lütjering, J. Williams, Titanium, Springer Berlin Heidelberg, Berlin, Heidelberg, 2007. https://doi.org/10.1007/978-3-540-73036-1.

[32] P. Samimi, P.C. Collins, Oxidation behavior of binary Ti-xW (0≤x≤30, wt%) alloys at 650°C as a function of W concentration, Corros Sci. 111 (2016) 531–540. https://doi.org/https://doi.org/10.1016/j.corsci.2016.05.038.

[33] T.M. Butler, K.J. Chaput, J.R. Dietrich, O.N. Senkov, High temperature oxidation behaviors of equimolar NbTiZrV and NbTiZrCr refractory complex concentrated alloys (RCCAs), J Alloys Compd. 729 (2017) 1004–1019. https://doi.org/10.1016/j.jallcom.2017.09.164.

[34] M. Kalienko, A. Volkov, M. Leder, A. Zhelnina, P. Panfilov, Study of lamination in beta-phase of Ti-5553 titanium alloy, in: IOP Conf Ser Mater Sci Eng, IOP Publishing, 2018: p. 012033. https://doi.org/10.1088/1757-899X/461/1/012033.

[35] J. Hendl, S. Daubner, A. Marquardt, L. Stepien, E. Lopez, F. Brückner, C. Leyens, In Situ CT Tensile Testing of an Additively Manufactured and Heat-Treated Metastable ß-Titanium Alloy (Ti-5Al-5Mo-5V-3Cr), Applied Sciences. 11 (2021) 9875. https://doi.org/10.3390/app11219875.

[36] F. Golightly, F. Stott, G. Wood, The Influence of Yttrium Additions on the Oxide-Scale Adhesion to an Iron-Chromium-Aluminum Alloy, Oxidation of Metals. 10 (1976) 163–187. https://doi.org/10.1007/BF00612158.

[37] H.C. GRAHAM, H.H. DAVIS, Oxidation/Vaporization Kinetics of Cr2O3, Journal of the American Ceramic Society. 54 (1971) 89–93. https://doi.org/10.1111/j.1151-2916.1971.tb12225.x.

[38] S.D. Cramer, B.S. Covino, eds., Corrosion: Fundamentals, Testing, and Protection, ASM International, 2003. https://doi.org/10.31399/asm.hb.v13a.9781627081825.

[39] S. Schellert, M. Weber, H.J. Christ, C. Wiktor, B. Butz, M.C. Galetz, S. Laube, A. Kauffmann, M. Heilmaier, B. Gorr, Formation of rutile (Cr,Ta,Ti)O2 oxides during oxidation of refractory high entropy alloys in Ta-Mo-Cr-Ti-Al system, Corros Sci. 211 (2023) 110885. https://doi.org/10.1016/j.corsci.2022.110885.